VIV Fatigue Assessment by Extended Scaling of Model Test Results

by R. Peek[a], O. Sequeiros[b], J. Wu[c], M. Witz[d], D. Yin[c] and H. Lie[c]
a) Peek Solutions, Avinguda Sant Andreu 116-8B-2º-1ª, 08392 Sant Andreu de Llavaneres, Spain
b) Shell Global Solutions, International, Volmerlaan 6, 2280 AB Rijswijk ZH, The Netherlands
c) SINTEF Ocean, Strindvegen 4, NO-7465 Trondheim, Norway
d) Crondall Energy Subsea, 13 Bon-Accord Square, Aberdeen AB11 6DJ, United Kingdom

Abstract

A method is proposed for VIV fatigue assessment of pipeline spans and risers by direct scaling of model test results. Scaling approximations serve to extend the range of applicability of a limited number of VIV test data. Also, scaling is applied only for the dynamic portion of the response, with the static portion calculated by analysis, which then provides the conditions for scaling. Ultimately using the basic and extended scaling approximations described, the problem of a simply supported span, on uniform pipe subject to constant current velocity is approximately characterized by a single dimensionless parameter. As a result, for any ("prototype") span to be assessed, any VIV test with similar end conditions (e.g. simply supported) can be scaled to yield the prototype current velocity for which similarity is satisfied. To facilitate this, test data from recent, well-instrumented VIV tests on simply supported spans are processed yielding convenient and physically meaningful normalized parameters describing the test conditions and response. Fatigue damage rates from the scaling method are compared to those from the DNVGL-recommended assessment procedure and those from the frequency domain version of Vivana.

Keywords: riser, pipeline, VIV, scaling, similarity, fatigue

1 Introduction

In a 1979 review article on VIV, Sarpkaya [1] predicted that "It is a research area which will continue to challenge the imagination of both the experimentalist and the theoretician for generations to come." Researches' imagination does indeed continue to be challenged 42 years later, with no end in sight, especially when multi-mode response is involved: the need for VIV tests to further cover cases of practical importance remains, especially for higher Reynolds numbers [2]. Approximate methods, either by modal analysis and an empirical response function (as in [3]) or by (complex) frequency domain analysis with empirical excitation and added mass functions [4-8] still miss important effects, and sophisticated ones including 3D CFD are still not generally accepted, in part because validation studies (such as [9]) do not yet include the full range of conditions for which the simulation tool might be used in practice, and good predictions for one case, do not necessarily mean they are also good for another. As a result, considerable uncertainty remains about VIV amplitude predictions, and even more about the fatigue damage from such vibrations.

To better understand this uncertainty in VIV fatigue damage, a new fatigue assessment method based on extended scaling of model test results is developed. This requires model tests that are qualitatively similar to the prototype to be assessed, e.g. in that the shape of the current velocity profile is similar, or any strake coverage and gaps therein are geometrically similar. The method relies on scaling approximations that replace certain assumptions in exsisting assessment methods. The scaling approximations include the well-known (Von Kármán) beam theory for moderately large deflections with constant effective axial force, which is also used in analysis methods, the principle of local action, that the hydrodynamic force at any location along the pipeline depends on the motion at that location only, which has also been extensively used, though not in the way applied here, an apparently new approximation whereby the requirement for similarity in the axial force may be relaxed, as an approximation, where there is a clear dominant wavelength of the response, and others.

Whilst it is not possible to verify the validity of the scaling approximations with existing experimental data, what is possible and done in this paper is to (a) assess the accuracy of the structural scaling approximations by calculating dimensionless indicators, (b) calculate convenient non dimensional parameters representing three test programs carried out at Marintek (now SINTE Ocean) with high mode response and heavily instrumented pipes whereby the scaling method is easily applied to any simply supported span, with bare, uniform pipe subject to constant current along the length, and (c) compare the scaling predictions to those from existing analysis methods for an example prototype pipe.

If VIV assessment is seen as the art of combining experimental results with theory to estimate fatigue damage, with a spectrum of methods ranging from fully experimental to more fully theoretical, then this paper falls more on the experimental side, requiring experiments closer to the real thing, to more directly use the experimental results, rather than using them in calibrate approximate methods.

Generally, “Buckingham’s Π Theorem” [10,11] is cited for dimensional analysis, although he was not the first to use it. The theorem applies for a relationship between “physical quantities” which Buckingham calls an “equation”, but here is called a function, as in practice the function may be evaluated by interpolation between experimental data points. Quoting Buckingham’s terms, the premise to his theorem is that if a “complete” set of the “physical quantities” is used, then the function does not depend on the units used, even when the arguments to the function are only the numbers without their units, provided that those units are consistent, i.e. all units used are derived from the same basic ones. This implies that not any function is physically admissible. Buckingham’s Π Theorem then provides and justifies the method to reduce the physically admissible function to its core relationship between dimensionless variables, which are fewer than the original physical quantities by the number of independent (or basic) dimensions involved, which for VIV problems are 3 (e.g. length, time, and mass). If the function is to be determined empirically, such reduction is crucial to limit the scope of the required experimental investigation, and it has been extensively used in designing and interpreting VIV tests (see for example [2,12]). However, the choice of dimensionless variables is not unique.

Here a combination of dimensional analysis, and approximations is used to reduce the number of dimensionless parameters, selecting ones that are physically meaningful and are stable in the sense that that the dimensionless output parameters (i.e. those representing results of the tests) do not change very much with changes in the dimensionless input parameters (i.e. those controlled by the design and execution of the test). In particular, a normalized fatigue-equivalent bending strain or curvature $\tilde{\epsilon}_e$ is defined and calculated, which varies only weakly as a function of the normalized input parameters, and from which the fatigue damage rate for a prototype pipe can readily be determined. Thus, $\tilde{\epsilon}_e$ is a good parameter to report for VIV test programs in which bending strains are measured, as is done here for recent well-instrumented high-mode tests carried out at Marintek (currently SINTEF Ocean).

In contrast to [13], which seeks to explain changes in VIV response amplitude in terms of a normalized equivalent damping coefficient c^* on the “power-in” zone of the pipe, which accounts for hydrodynamic damping in the “power-out” zone as well as structural damping everywhere, this effort is aimed defining a complete set of parameters to predict the fatigue damage rate. Indeed, the bare pipe tests considered all have low c^* values, since there is no “power out” zone with hydrodynamic damping. “Power in” and “power out” zones are the result of features that must be included in the model test to satisfy similarity. Despite limiting test data considered to those with low c^* values, considerable variability remains, and it is this variability that is examined in this paper.

2 Nomenclature

2.1 *Terms*

“Arch action” refers to the phenomenon described in [14] whereby static displacements combined with axial restraint at the ends increases the natural frequencies, especially for mode 1.

The “dynamic component” or “dynamic portion” of a time series is the amount by which it differs from its average value in time during the steady-state VIV.

The “dynamic amplitude” of a time series is $\sqrt{2}$ times the standard deviation. For a purely harmonic signal that is also equal to the amplitude of the sinusoidal signal.

The “logarithmic standard deviation” is defined as the standard deviation of the natural logarithm of the quantity in question. For small values, it is approximately equal to the coefficient of variation.

“Mode 1” for a simply supported span refers to the vibration mode with a single lobe. Similarly, “Mode 2” refers to a mode with 2 lobes, etc.. Due to arch action, Mode 1 may have a higher natural frequency than Mode 2.

"Normalized" parameters are dimensionless parameters that arise from the scaling and are the same for model and prototype. The bending strain, for instance, is a dimensionless parameter, but not a normalized parameter in the scaling used.

"Pipe" for the VIV tests means a flexible composite cylinder.

The "prototype" refers to the pipe, span or riser to be assessed for VIV fatigue, as opposed to the model tests performed to measure the VIV response.

"Reference vibrations" (used to assess the accuracy of scaling approximations in Appendix C) are defined to be vibrations of amplitude D, at the Strouhal wavelength ($2L_{st}$) and frequency (f_{st}).

"Scaling assumptions" or "scaling approximations" refer to Assumptions (1) to (9), listed in Section 2.

"Selected tests" refers to those selected in Section 6.1 based on indicators of validity of the accuracy of the scaling approximations.

The "static component" or "static value" refers to the average value in time when it is applied to a measured quantity. When applied to derived parameters, it refers to a value calculated using the static values as input.

"Straked" means strake-covered.

The "theory for moderately large deflections" is the same as the Euler-Bernoulli beam theory, except that a nonlinear term is included in an approximate expression for the axial strain at the centroid of the beam. See Eq. (39) for the strain-displacement relation, and Eq. (5) for the equilibrium equation derived from it via the principle of virtual displacements. It is the beam theory equivalent of the Von Kármán plate theory.

2.2 Symbols

$(.)$	any variable written as $(.) = (\tilde{.})(.)_1$.
$(\tilde{.})$	normalized value of (.), i.e. a tilde denotes the normalized value.
$(.)_1$	unit value of (.), i.e. a subscript 1 denotes the unit value.
a_{fat}	constant that determines the fatigue resistance according to $N_{cf} = a_{fat}/S^n$ where N_{cf} is the number of cycles to failure, S the stress range, and n another fatigue resistance constant.
c_{as}	still water added mass coefficient, added mass per unit mass of water displaced by the pipe; $c_{as} = 1$ based on potential theory without seabed proximity effects.
c_d	drag coefficient; for VIV tests, this is determined based on static solution from Appendix B, using the measured axial forces under gravity loads only, and the time-averaged axial force under flowing conditions, assuming that c_d is constant along the length of the pipe.
c_{eff}	effective mass coefficient; $c_{eff} = m_{eff}/m_{dw} = c_{pipe} + c_{as}$.
c_p	velocity of sound in the water.
c_{pipe}	mass ratio, $c_{pipe} = m_{pipe}/m_{dw}$.
C_k	flexural-stiffness-proportional damping coefficient (contribution to bending moment from damping is C_k times that rate of change of curvature).
$\tilde{C}_k$	normalized flexural-stiffness-proportional damping coefficient.
D	outer pipe diameter including coatings.
E	Young's modulus for material in which fatigue damage is calculated.
EI	pipe flexural rigidity including contribution of coatings, if any.
EI_{eff}	effective flexural rigidity at zero effective axial force to match the stiffness at the dominant wavelength λ; see Eq. (21).
$\mathbf{f}_h$	hydrodynamic force per unit length acting on the pipeline.

$f_{nst,arch}$, f_{nst} natural frequency of the symmetric mode for which the natural frequency is closest to the Strouhal frequency, with and without including arch action, respectively.

f_{st} Strouhal frequency $f_{st} = S_tU/D = 1/T_{st}$.

g acceleration due to gravity ($9.81 m/s^2$), except that in Appendix B, it denotes the increase in length of the pipe over the span due to transverse displacements with ends axially fixed.

$I_{v'\phi'}$, $I_{\phi\phi}$ used in Appendix B only to denote integrals over the span of what appears as the subscript; see Eqs. (34) & (35).

k_x stiffness of axial spring at one end of the VIV test models considered. The other end is assumed to be fully fixed axially.

L span length, or any reference length that is similarly defined for model and prototype.

$\tilde{L}$ normalized span length, $\tilde{L} = L/x_1 = L/L_{st}$.

L_{ea} effective length for axial stiffness. As in [14], this is chosen such that when the pipe becomes longer by an amount Δg due to transverse displacements at the span considered, the corresponding change in axial force is $\Delta N = EA\ \Delta g/L_{ea}$. See Eq. (32) for the case when the pipe is axially restrained at one end, and restrained by an axial spring of stiffness k_x at the other.

L_{st} Strouhal length, used as unit length (x_1) in the normalization adopted, and given in Eq. (10).

m_{dw} mass per unit length of fluid displaced by the pipe, $m_{dw} = \pi\rho D^2/4$.

m_{eff} still-water effective mass per unit length of the pipe, $m_{eff} = m_{pipe} + c_{as}\ m_{dw}$.

m_{pipe} mass per unit length of the pipe, content and any coatings

m_{pw} mass per unit length of the pipe wall including any coatings, but not the content of the pipe (for the VIV test pipes, this is equal to m_{pipe})

n either the exponent in fatigue resistance curve according to which the increment in fatigue damage η per cycle at strain range $\Delta\epsilon$ is $\Delta\eta = (\Delta\epsilon/\epsilon_{fr})^n$ or the mode number of a simply supported span, defined as the number of lobes of the mode considered. In the former case, the API X' curve is used here for which n=3.74.

n_{st} mode number for the symmetric mode for which the natural frequency is closest to the Strouhal frequency f_{st}.

N static effective axial force during VIV; constant with respect to x and t; includes effect of all quasi-static loadings including the static component of the drag force due to current velocity U; for VIV tests N is calculated as the average over time (see Assumption (6)).

N_{dyn} dynamic amplitude of axial force as measured during VIV test.

$\tilde{N}$ normalized effective axial force; see Eq. (12).

N_g effective axial force under gravity loads alone (at zero current velocity).

N_{seq} stiffness-equivalent axial force, axial force for which a cable (with zero flexural stiffness) has the same resistance to sinusoidal displacements at the Strouhal half wavelength as the pipe with flexural stiffness EI and axial force N.

q_d static drag force per unit length on the pipe, $q_d = ½\ \rho\ U^2\ D\ c_d$.

q_g submerged weight per unit length of the pipe, $q_g = (c_{pipe} - 1)\ m_{dw}\ g$.

$\mathbf{q}$ vector of hydrodynamic force per unit length acting on the pipe (in y-z plane) excluding the inertial term associated with the still-water added mass.

$\tilde{\mathbf{q}}$ normalized hydrodynamic force per unit length excluding the inertial term associated with the still-water added mass, see Eq. (4).

R_ϵ radius from the center of the pipe cross section to the location where the bending strain is determined.

S	stress range considered for fatigue loading.
S_t	dimensionless parameter that defines the selected normalization; the normalizations are valid for any value of this parameter; taken to be equal to the Strouhal number.
t	time.
t_1	unit value for time, taken to be the Strouhal period, i.e. $t_1 = T_{st} = D/(S_t\, U)$.
$\tilde{t} = \tau$	normalized time, $\tau = \tilde{t} = t/T_{st}$.
T_{st}	Strouhal period, used as unit value for time, $T_{st} = t_1 = D/(S_t U)$.
$T_{exposure}$	exposure time during which fatigue damage accumulates; model test time during which approximately steady-state VIV response conditions prevail.
$\tilde{T}_{exposure}$	normalized exposure time $\tilde{T}_{exposure} = T_{exposure}/T_{st}$ = number of cycles at the Strouhal frequency.
U	current speed; in the y direction, i.e. horizontal and normal to the pipeline.
$\tilde{U}$	normalized current speed, $\tilde{U} = UT_{st}/D$.
u	axial pipe displacement component, i.e. component in the x direction.
u_{dyn}	dynamic part of axial displacement component u.
v	static displacement of the pipe in the static plane under the action of gravity force q_g and drag force q_d.
$\mathbf{v}$	static part of transverse displacements, including a vertical (z) component due to gravity and a lateral (y) one due to the drag force.
$\mathbf{w}$	transverse displacement vector in y-z plane, $\mathbf{w}=\mathbf{w}(x,t)$; it can be either the total transverse displacement, or the dynamic component; see the paragraph following Eq. (5).
w	transverse displacement component (displacement in the y or z direction); used in equations that are valid for both y and z directions.

$\mathbf{w}'$,$\mathbf{w}''$, etc. first, second, etc. derivatives of $\mathbf{w}=\mathbf{w}(x,t)$ with respect to x.

$\ddot{\mathbf{w}}$	second derivative of $\mathbf{w}=\mathbf{w}(x,t)$ with respect to t.
$\tilde{\mathbf{w}}$	normalized transverse displacement vector in y-z plane, $\tilde{\mathbf{w}}=\mathbf{w}/D$, $\tilde{\mathbf{w}}=\tilde{\mathbf{w}}(\tilde{x},\tilde{t})$.
$\tilde{w}$	y or z component of $\tilde{\mathbf{w}}$ (in an equation that is valid for both the y and z components).

$\tilde{\mathbf{w}}'$,$\tilde{\mathbf{w}}''$, etc. first, second, etc. derivatives of $\tilde{\mathbf{w}}=\tilde{\mathbf{w}}(\tilde{x},\tilde{t})$ with respect to $\tilde{x}$.

$\ddot{\tilde{\mathbf{w}}}$	second derivative of $\tilde{\mathbf{w}}=\tilde{\mathbf{w}}(\tilde{x},\tilde{t})$ with respect to $\tilde{t}$.
x	axial coordinate along the pipeline, chosen such that the span covers the interval $x \in (0,L)$.
x_1	unit value of the axial coordinate, taken to be the Strouhal length, i.e. $x_1 = L_{st}$.
$\tilde{x}$	normalized axial coordinate $\tilde{x}=x/x_1=x/L_{st}$.
y	lateral (horizontal) coordinate, transverse to the pipeline.
z	vertical coordinate, increasing upwards.
ΔN	a change in effective axial force.
$\Delta\epsilon$	strain range; maximum less minimum strain over a full cycle.
$\Delta\eta$	increment in fatigue damage η due to a cycle at strain range $\Delta\epsilon$.
ϵ	bending strain in the in line or cross flow direction.
$\tilde{\epsilon}$	normalized bending strain or curvature, $\tilde{\epsilon} = \epsilon/\epsilon_1 = \tilde{w}''$ (when normalized, curvature and bending strain are equal).
ϵ_1	unit value for bending strain, $\epsilon_1 = R_\epsilon D/L_{st}^2$.

ϵ_e — equivalent strain amplitude for which the fatigue damage rate for cycles at amplitude ϵ_e at the Strouhal frequency ($f_{st}=1/T_{st}$) matches the actual fatigue damage rate; see Eq. (18). The reported values are for the location where the dynamic strain amplitude is the highest.

$\tilde{\epsilon}_e$ — normalized fatigue-equivalent bending strain or curvature; see Eq. (19).

ϵ_{fr} — constant in S-N fatigue resistance curve Eq. (15); represents strain range at which Eq. (15) predicts failure in one cycle; related to a_{fat} by $a_{fat} = (E\epsilon_{fr})^n$.

ϵ_t — total dynamic strain including axial as well as bending contributions.

η — fatigue damage due to bending in the in line or cross flow direction; failure occurs when η reaches 1.

$\dot{\eta}$ — mean fatigue damage rate, for test data this is obtained by Rainflow counting, as described in Appendix A, i.e. it is the average value over time; the values reported in this paper are those at the location where the dynamic strain amplitude is the highest; this serves as an approximation to the location of the maximum fatigue damage.

$\tilde{\dot{\eta}}$ — normalized fatigue damage rate from Eq. (17).

$\dot{\eta}_1$ — unit value of fatigue damage rate from Eq. (17).

λ — dominant half wave length for the pipeline response, see Section 5.

ν — kinematic viscosity of fluid surrounding the pipe.

θ — angle from vertical of the plane in which pipe hangs under the action of the gravity force q_g and the (static) drag force q_d (see Appendix B).

ρ — density of fluid surrounding the pipe.

ψ — relative error indicators for the scaling assumptions/approximations developed in Appendix C; different ψ values are distinguished by subscripts; $\psi \ll 1$ when the scaling approximation is good.

$\psi_{arch,1}$ — relative increase in natural frequency for mode 1 due to arch action, defined as the natural frequency including arch action divided by that without arch action minus one. (Here the "mode 1" refers to the single lobe mode, even when, due to arch action, its natural frequency is higher than for mode 2.)

$\psi_{arch,st}$ — relative increase in natural frequency due to arch action for the symmetric mode for which the natural frequency not including arch action is closest to the Strouhal frequency $f_{st} = S_t\ U/D$.

ζ — modal damping ratio for a sinusoidal mode with half wavelength L_{st} based on the flexural-stiffness-proportional viscous damping included in the formulation.

3 Scaling Approximations and Formulation

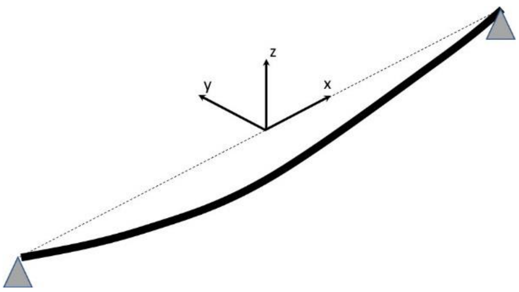

Figure 3.1 Span Coordinate System

For simplicity, the scaling is first developed for bare pipe of constant cross section over the length of the span shown in Figure 3.1 subject to a constant current velocity along its length. The purpose of scaling is to determine the VIV response and fatigue damage rate for a prototype pipe from VIV tests on a model pipe. For this, the static portion of the response for the prototype pipe is determined by analysis, using a drag coefficient that accounts for the effect of VIV. The scaling is then used for the dynamic portion of the response only.

The basic scaling assumptions are those used to derive the basic scaling result of this Section. They leave 3 normalized parameters to define a structurally-undamped, simply supported span. Extended scaling assumptions are developed in Section 5, but already stated in this Section, serve to further reduce the number of normalized problem parameters from 3 to 1.

Basic Hydrodynamic Assumptions/Approximations:

1) The water (or other fluid) is incompressible and fully characterized by its density ρ and kinematic viscosity ν. There is no cavitation or air entrainment.
2) The behavior is not sensitive to the viscosity of the fluid. I.e. the Reynolds number effect may be neglected, when the problem is nondimensionalized in such a way that the viscosity only appears in the Reynolds number.
3) The assumption of local action: The hydrodynamic force at any location is a function of the lateral and vertical displacement history $\mathbf{w}$ at that location only and is not affected by the motion $\mathbf{w}$ at other locations along the span.

Basic Structural Assumptions/Approximations:

4) The pipe remains linearly elastic, and the Euler-Bernoulli's beam approximation that plane sections remaining plane and normal to the axis of the pipe applies. Flexural-stiffness-proportional viscous damping is included.
5) Rotations of the pipeline remain small compared to 1 radian. This applies to static as well as dynamic rotations.
6) The axial force is constant along the length of the pipe, and dynamic changes in the axial force are neglected. I.e. arch action [14] is neglected. (Such arch action is mostly associated with the first vertical mode, but to a lesser extent it can also occur for higher modes. It requires axial restraint at the shoulders of the span and sag under gravity loads.) Also changes in axial force due to geometrically nonlinear effects such as those considered in [15] are neglected. (They are also not included in DNV's recommended span assessment practice [3].)
7) The axial inertia within the span length is neglected.

The accuracy of the approximations resulting from the above basic scaling assumptions is discussed in Appendix C. Although data suggest that Reynolds number do have an effect on VIV response [2,16], it is generally not practical to carry out model tests with high mode response at the right Reynolds number. Thus, Assumption (2) is more a matter of necessity, than justified by data or physical principles. In practice some allowance for Reynolds number effects not present in the scaled test may be appropriate. See data fitting efforts in Section 6.2 as well as Appendix C for further discussion of Reynolds number effects.

Extended Assumptions/Approximations:

In addition to the above basic scaling assumptions, the extended scaling assumptions that follow are used in Section 5, but not required for the basic scaling results of this section.

8) Certain effects associated with the pipe mass are neglected. This amounts to the same approximation as neglecting the effect of the mass ratio in the response functions of [3], and allows a model test for one mass ratio to be applied for another.
9) If a single half wavelength λ dominates the response, the stiffening effect of axial tension can be replaced by equivalent flexural rigidity and vice versa. This allows a model test at a different value of the normalized axial force $\tilde{N}$ to be applied.

In this section, the basic scaling results are derived using Assumptions (1) to (7) only.

First consider a forced vibration test in which a rigid cylinder undergoes a uniform motion $\mathbf{w} = D\,\tilde{\mathbf{w}}(t/t_1)$ in uniform flow of velocity U in the y direction (i.e. horizontal and normal to the cylinder). Here, t_1 should be regarded as any time scaling parameter. Changing it makes the normalized motion $\tilde{\mathbf{w}}(.)$ run faster or slower.

By the assumption of local action, the corresponding hydrodynamic force per unit length $\mathbf{f}_h$ does not depend of the length of the cylinder tested, but it does depend on the following: the dimensionless function $\tilde{\mathbf{w}}(.)$ that describes lateral as well as vertical motion, and the parameters ρ, ν, D, t, t_1 and U. Applying dimensional analysis (Buckingham's Π Theorem), this means that the normalized force $\tilde{f}_h = \mathbf{f}_h/[m_{dw} D/t_1^2]$ depends only on the dimensionless function $\tilde{\mathbf{w}}(.)$, the normalized time $\tilde{t} = t/t_1$ and the normalized current velocity $\tilde{U} = Ut_1/D$. In the above, $m_{dw} = \pi\rho D^2/4$ is the mass per unit length of fluid displaced by the pipe. The hydrodynamic force also depends on Reynolds number UD/ν but that effect is neglected by Assumption (3). Thus, $\tilde{\mathbf{f}}_h = \tilde{\mathbf{f}}_h(\tilde{t})$, where the function $\tilde{\mathbf{f}}_h(.)$ depends on $\tilde{\mathbf{w}}(.)$ and $\tilde{U}$.

The normalized motion $\tilde{\mathbf{w}}(.)$ can be any motion, such as the figure-of-8 or C-shaped motions observed in the VIV tests. There will be different motions $\tilde{\mathbf{w}}$ (.) at different locations x along the pipeline, but this scaling result can be applied to any of them.

To apply Assumption (8), the hydrodynamic force $\mathbf{f}_h$ is further decomposed into a linear term $-m_{dw}\, c_{as}\, \ddot{\mathbf{w}}$ that arises from the irrotational flow solution, plus a nonlinear term $\mathbf{q}$. Thus,

$$\mathbf{f}_h = \mathbf{q} - m_{dw}\, c_{as}\, \ddot{\mathbf{w}} \tag{1}$$

where c_{as} is the added mass coefficient from the irrotational flow solution, which is $c_{as} = 1$ in absence of seabed proximity effects, and $\ddot{\mathbf{w}}$ denotes the second derivative of $\mathbf{w}$ with respect to time t. In normalized form, this equation can be written as

$$\tilde{\mathbf{f}}_h = \tilde{\mathbf{q}} - c_{as}\, \ddot{\tilde{\mathbf{w}}} \tag{2}$$

where $\tilde{\mathbf{q}} = \mathbf{q}/[m_{dw} D/t_1^2]$ is the normalized nonlinear component of the hydrodynamic force, and $\ddot{\tilde{\mathbf{w}}}$ is the second derivative of $\tilde{\mathbf{w}}(.)$ with respect to its argument $\tilde{t}$. It follows that, for a given value of c_{as}, $\tilde{\mathbf{q}} = \tilde{\mathbf{q}}(\tilde{t})$, where the function $\tilde{\mathbf{q}}(.)$ depends only on $\tilde{\mathbf{w}}(.)$ and $\tilde{U}$.

Applying this and the approximation of local action (Assumption (2)), for a motion

$$\mathbf{w}(x,t)=D\, \tilde{\mathbf{w}}(x/x_1,t/t_1) \tag{3}$$

the corresponding hydrodynamic force can be written as

$$\mathbf{f}_h(x,t) = m_{dw}\, (\tilde{\mathbf{q}}(x/x_1,t/T)\, D/t_1^2 - c_{as}\, \ddot{\mathbf{w}}) \tag{4}$$

where the function $\tilde{\mathbf{q}}=\tilde{\mathbf{q}}$ (.,.) depends only on the function $\tilde{\mathbf{w}}(.,.)$ and the normalized current velocity $\tilde{U}=Ut_1/D$.

Further simplification is achieved by the structural Approximations (4) to (7). With these, the equation of motion for the lateral and vertical displacements $\mathbf{w}$ reduces to

$$EI\ \mathbf{w}'''' - N\,\mathbf{w}'' + C_k\, \dot{\mathbf{w}}'''' + m_{pipe}\, \ddot{\mathbf{w}} = \mathbf{f}_h \quad \forall\ x \in (0,L) \tag{5}$$

where EI is the flexural stiffness, N the effective axial tension, and C_k a damping coefficient associated with flexural deformations of the pipe.

Eq. (5) applies for the dynamic portion of the response $\mathbf{w}=\mathbf{w}(x,t)$ and the corresponding hydrodynamic force per unit length $\mathbf{f}_h$ which the fluid exerts on the pipe. A similar equation applies to the static portion, except that the inertia and damping term is absent, and the static load also includes the gravity force acting on the pipe in addition to the static portion of the force $\mathbf{f}_h$ exerted on the pipe by the surrounding fluid.

It follows from Assumptions (4) to (7) and momentum balance in the axial direction that N is constant with respect to location x along the span as well as in time t. N is determined based on static analysis considering gravity forces and hydrodynamic drag.

In the above, "the static portion" refers to the time-averaged value and the dynamic portion is what remains. The increase in drag force due to VIV should also be included in the static analysis.

The effective axial force N includes a contribution from the hydrostatic external pressure. This accounts for changes in area exposed to external pressure under bending deformations that should not be included in $\mathbf{f}_h$ as well.

Substituting Eqs. (3) and (4) into Eq. (5) to write the governing equation in terms of the normalized functions $\tilde{\mathbf{w}}(\tilde{x}, \tilde{t})$ and $\tilde{\mathbf{q}}(\tilde{x},\tilde{t})$, one obtains

$$(EI\ D/x_1^4)\ \tilde{\mathbf{w}}'''' - (N\ D/x_1^2)\ \tilde{\mathbf{w}}'' + (C_k\ D/(t_1\ x_1^4))\ \dot{\tilde{\mathbf{w}}}'''' + (m_{eff}\ D/t_1^2)\ \ddot{\tilde{\mathbf{w}}} = (m_{dw}\ D/t_1^2)\ \tilde{\mathbf{q}} \tag{6}$$

which applies for all $\tilde{x} \in (0,\tilde{L})$. When applied to $\tilde{\mathbf{w}}$, the primes and dots denote differentiation with respect to the normalized axial coordinate $\tilde{x} = x/x_1$ and time $\tilde{t} = t/t_1$, respectively. See Nomenclature for explicit definitions.

Equation (6) is valid for any t_1 and x_1. Different choices of these unit values lead to different normalizations. To facilitate physical interpretation of the normalized parameters that will arise, t_1 and x_1 are taken to be the Strouhal period and length, T_{st} and L_{st}, respectively, defined by

$$t_1 = T_{st} = D/(S_t U) \tag{7}$$

$$(\pi/L_{st})^4\ EI + (\pi/L_{st})^2\ N = m_{eff}\ (2\pi/T_{st})^2 \tag{8}$$

Thus L_{st} represents the length of a simply supported span for which the still-water natural frequency is equal to the Strouhal frequency S_t U/D. The 2nd equation above is a quadratic in $(\pi/L_{st})^2$, which always has one positive root given by

$$(\pi/L_{st})^2 = \{[N^2 + 16\pi^2\ EI\ m_{eff}/T_{st}^2]^{1/2} - N\}/(2EI) \tag{9}$$

so that

$$x_1 = L_{st} = \pi\ (2EI)^{1/2}/\{[N^2 + 16\pi^2\ EI\ m_{eff}/T_{st}^2]^{1/2} - N\}^{1/2} \tag{10}$$

Simplifying (6) for the normalization defined by Eqs. (7) to (10) gives

$$\{4\ c_{eff}/[\pi^2(1 + \tilde{N})]\}\ (\tilde{\mathbf{w}}'''' - \pi^2\tilde{N}\ \tilde{\mathbf{w}}'') + c_{eff}\ \ddot{\tilde{\mathbf{w}}} = \tilde{\mathbf{q}} - (4/\pi^5)\ \tilde{C}_k\ \dot{\tilde{\mathbf{w}}}'''' \qquad \forall\ \tilde{x} \in (0,\tilde{L}) \tag{11}$$

where

$$\tilde{N} = N/N_1,\ \ N_1 = \pi^2 EI/L_{st}^2,\ \ \tilde{L} = L/L_{st}\ ,\ \ \tilde{C}_k = \pi^3\ C_\kappa\ c_{eff}/[EI\ T_{st}\ (1+\tilde{N})] \tag{12}$$

In the above $\tilde{C}_k$ is a normalized damping parameter that reflects the flexural-stiffness-proportional damping included in the formulation. This parameter has been defined in such a way that for a simply supported span of length L_{st}, $\tilde{C}_k$ is the Scruton mass-damping parameter, which is referred to as the “stability parameter” and denoted by “K_S” in [3]. The modal damping ratio for a mode with half wavelength L_{st} is $\zeta = \pi^2\ c_{pipe}\ \tilde{C}_k$.

It follows from Eq. (7) and the definition of the normalized current speed $\tilde{U}$ following Eq. (4) that

$$\tilde{U} = 1/S_t \tag{13}$$

The above results are valid for any value of S_t. Only the interpretation of T_{st} and L_{st} as the Strouhal period and length relies on S_t being taken to be the Strouhal number. Here S_t=0.2 is used as a reference value throughout. This results in $\tilde{U}$=5. Although and empirical relation between Strouhal and Reynolds number is well-documented [17], the same value of S_t must be used for model and prototype for the scaling laws developed here to be valid. If Reynolds number effects are important, the only way to properly account for them is to perform the model test at the Reynolds number of the prototype.

Now suppose a model test is performed for given values of the input parameters D, EI, C_k, L, m_{eff}, N, U and ρ. Then, the normalized solution $\tilde{\mathbf{w}} = \tilde{\mathbf{w}}(\tilde{x},\tilde{t})$ derived from this model also applies to a prototype with different values of the input parameters provided that the normalized input parameters $\tilde{N}$, c_{eff}, $\tilde{L}$ and $\tilde{C}_k$ are the same for model and prototype. Of course similarity in the boundary conditions must also be satisfied. For the cases covered in Table 3.1, this means the normalized stiffness coefficients $\tilde{k}$ or $\tilde{k}_{ij}$ in Table 3.1 must be the same for the model and the prototype.

For real spans with the pipe supported by soil at the shoulders, the boundary conditions are complex: they are nonlinear and inelastic due to soil plasticity and possible loss of contact. However in VIV tests, the ends are often simply supported. That is the case for all VIV tests reported in this paper. For the tests with strake-covered pipes and a gap in the strake coverage at midspan, the response tends to decay towards the shoulders, so the exact boundary conditions may not be that important for such cases.

For the undamped, pinned-pinned or fixed-fixed case, there are 7 problem input parameters, leading to only 3 normalized problem input parameters. The means that an experimental program to cover cases of engineering interest needs to cover a 3-dimensional region of interest in the normalized parameter space. It requires far fewer experiments to cover the 3-dimensional normalized parameter space than to cover the 7-dimensional space of actual input parameters. Here "cover" means fill the space with a grid of experimental points, that are sufficiently closely-spaced that one can interpolate between the points. For example, if 10 points are sufficient to capture the range of values of engineering interest of each parameter, it requires 10^3 tests to cover the normalized parameter space instead of 10^7 to cover the actual parameter space. However, it still takes a larger number of tests than are currently available to cover the 3-dimentional normalized space. A further reduction to just one input parameter, the normalized span length $\tilde{L}=L/L_{st}$, is achieved in Section 5 using Assumptions (8) and (9).

A similar scaling result could be derived purely by dimensional analysis using Eq. (5) only to identify the "complete" list of "physical quantities" [10] for which a "physical equation" exists as ρ, ν, D, m_{pipe}, EI, C_k, N, L, U i.e. 9 "physical quantities" which can be reduced to 6 normalized parameters $\tilde{L}$, $\tilde{N}$, $\tilde{C}_k$, c_{pipe}, DU/ν, D/L. The only difference is D/L, which the more detailed analysis above has eliminated using local action.

Having obtained the normalized solution, the bending strain can be calculated from

$$\epsilon = w'' R_\epsilon = \epsilon_1 \tilde{\epsilon}\,, \quad \tilde{\epsilon} = \tilde{w}''\,, \quad \epsilon_1 = R_\epsilon D/L_{st}^2 \tag{14}$$

For the fatigue resistance, Miner's rule is applied, and it is assumed that the S-N curve is linear when plotted on a log-log scale. This means that fatigue failure occurs when the fatigue damage reaches 1, and the increment Δη in fatigue damage per cycle at strain range Δϵ can be written as

$$\Delta\eta = (\Delta\epsilon/\epsilon_{fr})^n \tag{15}$$

where ϵ_{fr} and n are constants that define the S-N fatigue resistance curve. The total fatigue damage η is obtained by summing the damage for each cycle identified by a Rainflow algorithm, and the mean fatigue damage rate can be written as

$$\dot{\eta} = \Sigma_{rainflow} (\Delta\epsilon/\epsilon_{fr})^n / T_{exposure} = \dot{\eta}_1 \tilde{\dot{\eta}} \tag{16}$$

where $\Sigma_{rainflow}$ denotes the sum over all strain ranges Δϵ identified by the rainflow counting algorithm used[1] over an exposure time $T_{exposure}$, $\dot{\eta}_1$ and $\tilde{\dot{\eta}}$ are the unit value, and normalized value, respectively, of the fatigue damage rate $\dot{\eta}$, given by

[1] The rainflow algorithm used for the experimental data reported here is "Algorithm 1" from [25], with details of its application given in Appendix A.

$$\dot{\eta}_1 = [\epsilon_1/\epsilon_{fr}]^n / T_{st}, \qquad \dot{\tilde{\eta}} = \Sigma_{rainflow} \Delta\tilde{\epsilon}^n / \tilde{T}_{exposure} \tag{17}$$

where $\Delta\tilde{\epsilon}$ is the range of the normalized strain $\tilde{\epsilon} = \tilde{w}''$, and $\tilde{T}_{exposure} = T_{exposure}/T_{st}$.

Note that ϵ is a dimensionless but not a normalized parameter. For the same normalized solution, there can be different values for the bending strain ϵ for the model and the prototype.

Whereas $\dot{\tilde{\eta}}$ is a properly normalized fatigue damage rate, it has two disadvantages when it comes to presenting the test results in normalized form: (i) the numbers turn out to be large, and (ii) they are sensitive to the fatigue exponent n. Those drawbacks can be overcome by defining a fatigue-equivalent strain amplitude ϵ_e such that the fatigue damage rate for strain cycles of constant amplitude ϵ_e at the Strouhal frequency is that same as the actual fatigue damage rate $\dot{\eta}$. Thus,

$$\dot{\eta} = (2\epsilon_e/\epsilon_{fr})^n/T_{st}, \qquad \epsilon_e = ½\, \epsilon_{fr}\, (T_{st}\, \dot{\eta})^{1/n} \tag{18}$$

Or in normalized form,

$$\dot{\tilde{\eta}} = (2\tilde{\epsilon}_e)^n, \quad \tilde{\epsilon}_e = \epsilon_e/\epsilon_1 = ½\, (\dot{\tilde{\eta}})^{1/n} \tag{19}$$

For a given VIV test, this fatigue-equivalent normalized strain amplitude $\tilde{\epsilon}_e$ also depends on the fatigue exponent n, but the dependence is much weaker than for $\dot{\tilde{\eta}}$. As such, as an approximation, $\tilde{\epsilon}_e$, values may be used to calculate fatigue damage rates in prototype pipes for slightly different values of the exponent n for which the $\tilde{\epsilon}_e$ values are derived from the model tests.

Description	Formulation	Normalized Formulation
Pinned-Pinned	$w = 0$, $w''=0$ at $x=0,L$	$\tilde{w} = 0$, $\tilde{w}''= 0$ at $\tilde{x}=0,\tilde{L}$
Fixed-Fixed	$w = 0$, $w'=0$ at $x=0,L$	$\tilde{w} = 0$, $\tilde{w}'=0$ at $\tilde{x}=0,\tilde{L}$
Coupled linear rotational and transverse spring shoulders with same properties for the shoulders on both sides	At $x=0$: $-N\,w' + EI\,w''' = k_{11}\,w - k_{12}\,w'$ $-EI\,w'' = k_{12}\,w - k_{22}\,w'$ At $x=L$: $N\,w' - EI\,w''' = k_{11}\,w + k_{12}\,w'$ $EI\,w'' = -k_{12}\,w - k_{22}\,w'$ where k_{ij} are the components of a 2 × 2 stiffness matrix for the boundary at the span shoulder. The point directions are 1 for displacements w, and 2 rotations –w'. (Here the same shoulder stiffness matrix is assumed for the vertical and lateral directions with the resistances for these directions assumed to be uncoupled. A more general linearized boundary stiffness could also readily be defined, but results in a greater number of distinct normalized stiffness coefficients.)	At $\tilde{x}=0$: $-\tilde{N}\,\tilde{w}' + \tilde{w}''' = \tilde{k}_{11}\,\tilde{w} - \tilde{k}_{12}\,\tilde{w}'$ $-\tilde{w}'' = \tilde{k}_{12}\,\tilde{w} - \tilde{k}_{22}\,\tilde{w}'$ At $\tilde{x}=\tilde{L}$: $\pi^2\,\tilde{N}\,\tilde{w}' - \tilde{w}''' = \tilde{k}_{11}\,\tilde{w} + \tilde{k}_{12}\,\tilde{w}'$ $\tilde{w}'' = -\tilde{k}_{12}\,\tilde{w} - \tilde{k}_{22}\,\tilde{w}'$ where $\tilde{k}_{11} = k_{11}\,L_{st}^3/EI$ $\tilde{k}_{12} = k_{12}\,L_{st}^2/EI$ $\tilde{k}_{22} = k_{22}\,L_{st}/EI$
Continuation of the pipe model beyond the shoulder on a bed of springs of stiffness k.	Governing equation for soil-supported region beyond the shoulder becomes Eq. (5) with an additional term k w on the left hand side.	The additional term of the left hand side of Eq. (11) becomes $\tilde{k}\,\tilde{\mathbf{w}}$, where $\tilde{k} = kL_{st}^4/EI$.

Table 3.1 Examples of simple boundary conditions that can be applied at the shoulder of the span and their normalization. For similarity between model and prototype, the normalized boundary parameters $\tilde{k}$ or $\tilde{k}_{ij}$ must be the same for model and prototype.

4 Partially Strake-Covered Pipe

So far the basic scaling results have been derived for bare pipe of a uniform cross section along the length of the pipe. However, the same applies for partially straked pipe, provided the strake coverage, and the strakes themselves are similar for model and prototype. For instance if strakes with a pitch of 15D and a height of 0.25D cover the entire span except a gap of 25% of the span length centered at midspan, the same must be the case for the model.

In this case the parameters D, EI, m_{pipe} and m_{dw} are chosen to reflect the bare pipe, whereas c_{as} is allowed to change as a function of location, so that in any straked portions of the pipe it accounts for any additional added mass due to the strakes. It can also account for the increase in diameter due to the strakes and the mass of the strakes themselves. All arguments of Section 2 still apply, except that c_{as} and c_{eff} now vary as a function of location along the pipe.

5 Further Simplifications

If one wants to assess VIV for a prototype and has a model test with the same values of $\tilde{L}$, $\tilde{C}_k$, c_{eff}, and $\tilde{N}$, no further approximations are required. The further approximations described in this section allow the VIV test to be used even if only $\tilde{L}$ and $\tilde{C}_k$ match but not c_{eff} and/or $\tilde{N}$. This is based on Assumptions (8) and (9) from Section 2.

First consider c_{eff} and Assumption (8). The mass ratio must satisfy $c_{pipe} \geq 1$ or the pipe would float to the surface. Typical mass ratios for gas lines are in the range $c_{pipe} \in (1.1, 1.4)$. Further, in absence of seabed proximity effects, $c_{as} = 1$. This means that the effective mass coefficient $c_{eff} = c_{pipe} + c_{as}$ is in the range $c_{eff} \in (2.1, 2.4)$. The extremes of this range differ by less than 10% from its middle. On this basis alone, a model test in this c_{eff} range provides a reasonable approximation any prototype in the same range.

Further, the normalized equation of motion Eq. (11) contains c_{eff} only on as a factor multiplying all terms on the right hand side. The right hand side is zero for undamped free vibration response. The normalized frequency of that response is not affected by c_{eff}. The terms that include energy input and dissipation are on the right hand side. These are also unaffected by c_{eff} in the sense that c_{eff} will not affect the balance between energy input and dissipation. These observations suggest the effect of c_{eff} on the normalized solution is limited. (Note that the effect of mass on VIV via the natural frequency is accounted for even when the effect of c_{eff} on the normalized solution is neglected.)

Finally, neglecting the effect of c_{eff} on the normalized solution corresponds to neglecting the effect of the mass ratio on the normalized VIV response amplitude. This is the approximation adopted in DNV's Recommended Practice [3] after extensive calibration efforts using experimental data. It suggests that the experimental data also show a limited effect of c_{eff}, or at least that it is conservative to use the estimated response for mass ratios near 1 for higher mass ratios. (Pipe-in-pipe systems for high pressure deepwater fields could have mass ratios well above $c_{pipe} = 1.4$.) Indeed, tests reported in [18] do show a considerable reduction in response for high mass ratios, except at the peak of the response when plotted as a function of reduced velocity. See Fig. 3 of [18]. This peak also corresponds to point where the Strouhal frequency coincides with the natural frequency of the span.

Assumption (9) eliminates the similarity requirement for the normalized axial force $\tilde{N}$. That requires an approximation that is valid when the response has a clear dominant wavelength. If the axial tension is so high that the effect of flexural rigidity is comparatively small even for the shorter wavelengths of the response, this will be a good approximation even if several wavelengths contribute significantly to the response. Whereas Assumption (8) (regarding c_{eff}) is also in [3] and, as a result, is much used in practice, the authors are not aware of any previous statement or use of Assumption (9).

To use Assumption (9), it is necessary to estimate the dominant half wavelength (denoted by λ) from the model test data. Different ways are used to estimate this from the available model test data, as described in Section 8.2. Having obtained λ for the model, the prototype value is readily determined since λ/L and $\tilde{\lambda}=\lambda/L_{st}$ must be the same for model and prototype.

If the half wavelength λ is indeed dominant, both the axial force N and the flexural rigidity EI for the prototype can be adjusted in such a way that (i) the correct resisting force is developed for sinusoidal displacements at the dominant wavelength and (ii) using the adjusted values of N and EI (denoted by N_{adj} and EI_{adj}) for the prototype, the corresponding normalized axial force $\tilde{N}$ for the model and prototype are the same.

For a displacement $\sin(\pi x/\lambda)$, the corresponding transverse force per unit length from the first two terms in Eq. (5) is $[EI\,(\pi/\lambda)^4 + N\,(\pi/\lambda)^2]\,\sin(\pi x/\lambda)$. This is the same as one gets at zero effective axial force with a flexural rigidity given by

$$EI_{eff} = EI + N\,(\lambda/\pi)^2 \tag{20}$$

The requirements (i) and (ii) above yield the following adjusted values for the adjusted flexural rigidity EI and effective axial force N:

$$EI_{adj} = EI_{eff}/(\tilde{\lambda}^2 + \tilde{N}), \quad N_{adj} = \tilde{N}\,\pi^2 EI_{adj}/L_{st}^2 \tag{21}$$

This adjustment is carried out for the prototype using the value of $\tilde{N}$ for the model. All calculations for the prototype to determine the motion $\mathbf{w}=\mathbf{w}(x,t)$ are carried out with the adjusted values of EI, and N. This also yields the curvatures $\mathbf{w}''$ and corresponding bending strains $\epsilon = R_\epsilon\, w''$. The unadjusted EI and N are used to calculate the bending moments EI $\mathbf{w}''$ and the static solution under gravity and drag loads.

6 VIV Test Data

6.1 Test Definition and Selection

To experimentally verify the basic scaling approximations requires VIV test data for which the normalized parameters $\tilde{L}$, $\tilde{N}$ and c_{pipe} are the same, while other parameters (such as D/L) are different. In lieu of a dedicated test program, such data are not available. Instead, available data from well-instrumented, high-mode tests are used. Although this does not lead to an experimental verification of the scaling approximations, it does lead to a range of normalized values for the dynamic, and normalized fatigue-equivalent strain amplitudes, $\tilde{\epsilon}_e$, which are useful in estimating fatigue damage rates for practical cases, and the uncertainty therein.

The tests considered are high-mode VIV tests on simply-supported spans performed at Marintek (now SINTEF Ocean). The spans are "towed" in still water to simulate the current. Three different test programs are considered: "EM" tests sponsored by ExxonMobil described in [19] with data available from [20] on a vertical riser model that undergoes a slightly curved path in the still water, as the rig rotates about a vertical axis, "OL" tests sponsored by the Ormen Lange project lead by Norske Hydro [21], and on "Pipe 1" to "Pipe 3", with different diameters, sponsored by Shell [22,23]. Key test parameters shown in Table 6.1 together with ranges of results.

Although some of the programs included cases with "sheared current" (i.e. towing speed changing along the length of the model by using a rotating rig), as well as various VIV suppression devices, here attention is focused on tests without suppression devices in which the current is constant along the length of the span.

The models are hinged at the ends for both axes of bending, but restrained against torsion and transverse translation. Axially they are fixed at one end, and at the other the tension is maintained by an axial spring. As a result, the static tension increases under the drag loads from N_g to N, and this measured change is used according to the formulation in Appendix B to estimate the angle θ from vertical at which the pipe hangs, and the effective drag coefficient, c_D, assuming that the drag is constant along the length of the pipe.

The Shell pipes also have 500kg clump weights at the ends of the model, to stabilize the ends. The hinges at the ends are between the clump weights and the pipe. They only allow relative rotations in the two bending directions. The rig design principle is that, in lieu of enough stiffness of the supporting structure, the mass of the clumps is high enough so that the natural frequency for vibrations of the clumps is low compared to the VIV frequencies, and thus the clumps suppress transverse movement at the ends. However, in the axial direction, the pipe is relatively stiff, and this gives rise to a natural frequency involving the clumps on each side moving in opposite directions with alternating extension and contraction of the pipe. For that mode, the natural frequency can fall in the range of the VIV frequencies. How this might affect the behavior is further considered in Appendix C.

All tests are heavily instrumented, and include measurement of the bending strain at many locations along the pipe and the axial force at one end of the pipe. In some cases accelerometers are also included from which displacements can be determined at several points along the pipe. However, since displacement measurements are not available for all cases, attention here is focused on the strains, which are also the most relevant parameter for fatigue assessment.

For each test, the part of the record over which a steady state appears to have been achieved is selected, and the results are presented in terms of the *static* value (which corresponds to the average in time taken over the selected steady-state portion of the record), and the *dynamic amplitude* (which is defined as $\sqrt{2}$ times the standard deviation of the steady state portion of the time series). If the response is purely harmonic this dynamic amplitude is equal to the amplitude of the sinusoidal variation.

The average fatigue damage rate $\dot{\eta}$ is determined by rainflow counting (as described in Appendix A) over the steady state portion of the record. This is performed at the cross flow and in line location where the dynamic amplitude of the strain is the largest. (The maximum fatigue damage rate and the maximum dynamic amplitude of the strain do not necessarily occur at the same location, but to reduce processing effort, the adopted approach can be considered to provide an approximation to the spatial maximum of the average in time of the fatigue damage rate.)

From the experimental results, the normalized parameters of Section 2 can readily be calculated. Further dimensionless parameters ψ defined in Appendix C that give an indication of the relative errors arising from the scaling approximations are calculated. Of these two are used to eliminate data for which such errors are judged too large.

Firstly data for which the measured dynamic axial force is judged too high are excluded. For this, the dynamic axial force ratio given by

$$\psi_N = N_{dyn}/N_{seq} \tag{22}$$

is used, where N_{dyn} is the dynamic amplitude of the axial force as determined from the VIV test records, and N_{seq} is given by

$$N_{seq} = N + \pi^2 EI/L_{st}^2 \tag{23}$$

and represents the stiffness-equivalent axial force, for which the stiffness to restore out of straightness as the Strouhal wavelength is the same for a cable under tension N_{seq} as for the pipe under tension N. Only data with $\psi_N \leq 0.1$ are included.

Secondly, $\psi_{arch,st}$, quantifies the effect of arch action on the symmetric mode for which the natural frequency not including arch action is closest to the Strouhal frequency. (Antisymmetric modes are not affected by arch action.) It is defined by

$$\psi_{arch,st} = f_{nst,arch}/f_{nst} - 1 \tag{24}$$

where $f_{nst,arch}$ and f_{nst} are defined as the natural frequencies of the symmetric mode for which the natural frequency not including arch action is closest to the Strouhal frequency in still water with and without considering arch action, as calculated based on [14] as described in Appendix B, respectively. Only data with $\psi_{arch,st} \leq 0.1$ are included. I.e. if arch action increases the natural frequency by more than 10% the test is excluded. Data exclusions based on ψ_N and $\psi_{arch,st}$ are illustrated in Figure 6.1.

Further, data are excluded for which the calculated[2] static rotation at the ends under flowing conditions exceeds 0.4 radians, as illustrated in Figure 6.2 for the data not excluded by the ψ_N and $\psi_{arch,st}$ criteria.

The intent of the exclusions is that the remaining data should satisfy Assumptions (5) to (7), at least approximately. Of 111 VIV tests on bare pipe, 73 remain after the exclusions according to the criteria in Figure 6.1 and Figure 6.2. Except for Figure 6.1 and Figure 6.2, all other plots of test data and results in Table 6.1 cover only the included tests.

The normalized span length and axial force values, $\tilde{L}$ and $\tilde{N}$, respectively for the included tests are plotted in Figure 6.3. Although one could design a test program in which $\tilde{L}$ and $\tilde{N}$ are varied independently, that is not the case for the available data: For the OL and EM tests, only the current velocity is varied from one test to the next. As the velocity increases, the Strouhal half wavelength L_{st} decreases. This causes $\tilde{L}$ to increase and $\tilde{N}$ to decrease. The latter is only partly compensated by the increase in axial force due to the increased drag. For the (Shell-sponsored) Pipe 1 to 3 tests, the axial force under gravity alone is not the same from test to test on the same pipe. As a result, the points in Figure 6.3 for each of these pipes do not fall on a smooth line.

The Reynolds numbers covered by the tests are shown in Figure 6.4, which also show how the Reynolds number changes simultaneously with $\tilde{L}$ within each test series, as changes are made to the "towing" speed for a given pipe.

Figure 6.3 also shows that there no test series on different pipes with the same $\tilde{L}$ and $\tilde{N}$ values, except for tests on rough and smooth versions of Pipe 3 at $(\tilde{L},\tilde{N})=(3.9,109)$. The closest it gets for different pipes is shown within the box in Figure 6.3, where one Pipe 1 test is close to several Pipe 2 tests.

---

2 Calculated as described in Appendix B, but where the measured static axial force under flowing conditions does not exceed that under still water conditions, a drag coefficient of $c_d = 1.4$ is used.

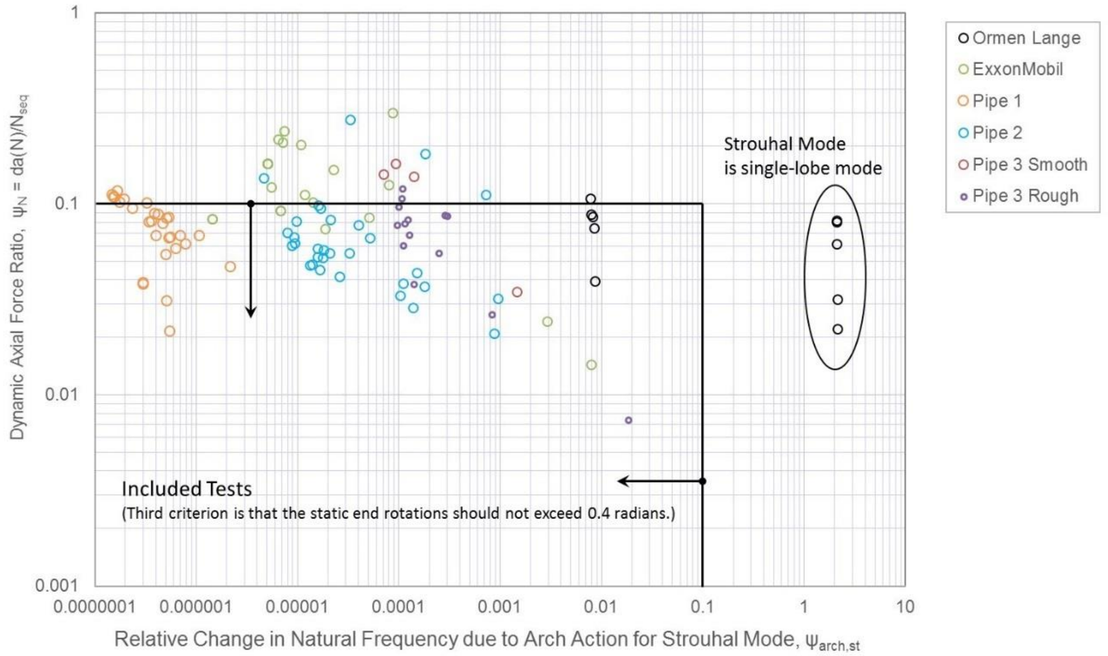

Figure 6.1 **Exclusion of tests for which the dynamic axial force exceeds 10% of the stiffness-equivalent axial force N_{seq} or arch action increases the natural frequency of the symmetric mode for which the natural frequency not including arch action is closest to the Strouhal frequency by more than 10%. A third criterion, not shown on this figure is that the calculated static rotations at the ends under flowing conditions should not exceed 0.4 radians.**

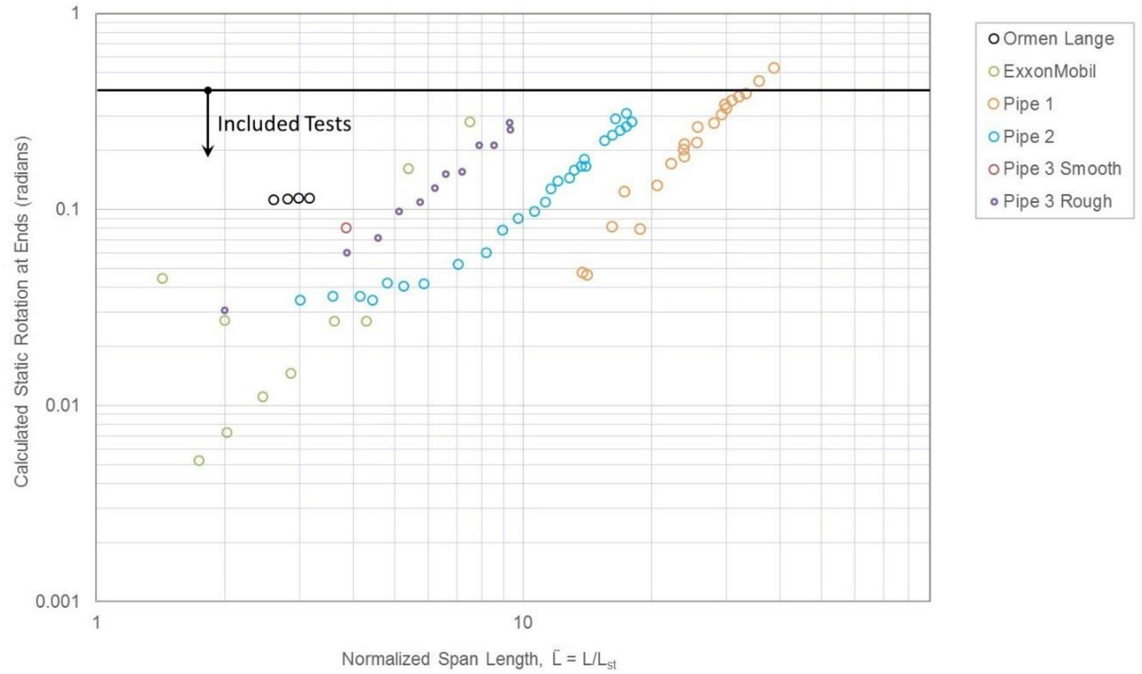

Figure 6.2 **Static rotations for test data not excluded by the criteria of Figure 6.1.**

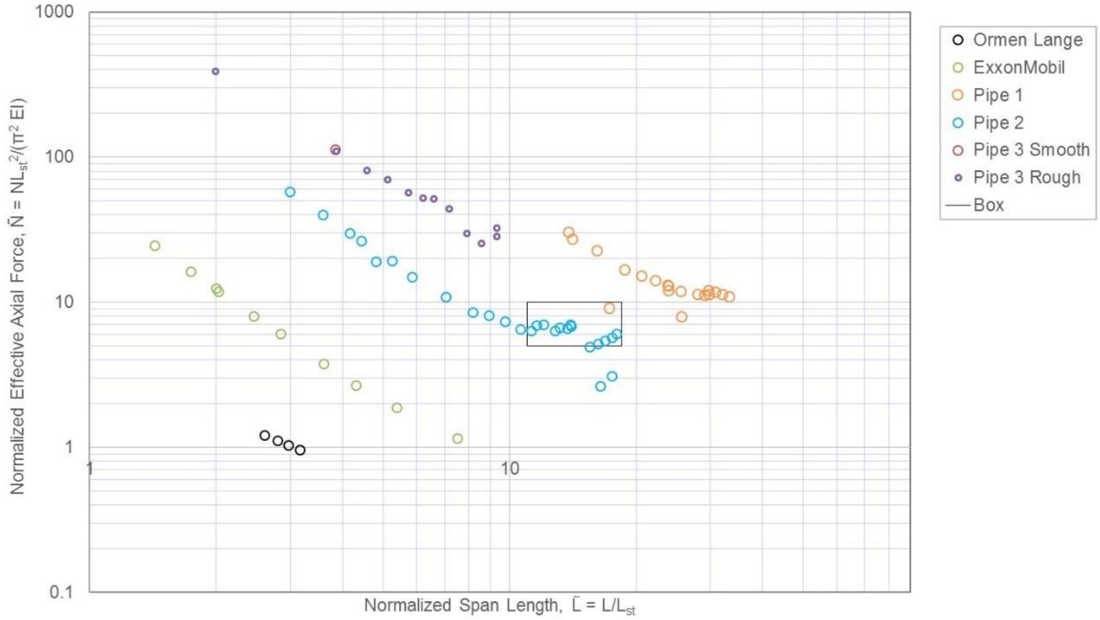

Figure 6.3 Calculated normalized span lengths and axial forces, L̃ and Ñ, respectively for the included test data (on bare pipe under uniform current with $\psi_{arch,st} \leq 0.1$ and $\psi_N \leq 0.1$)

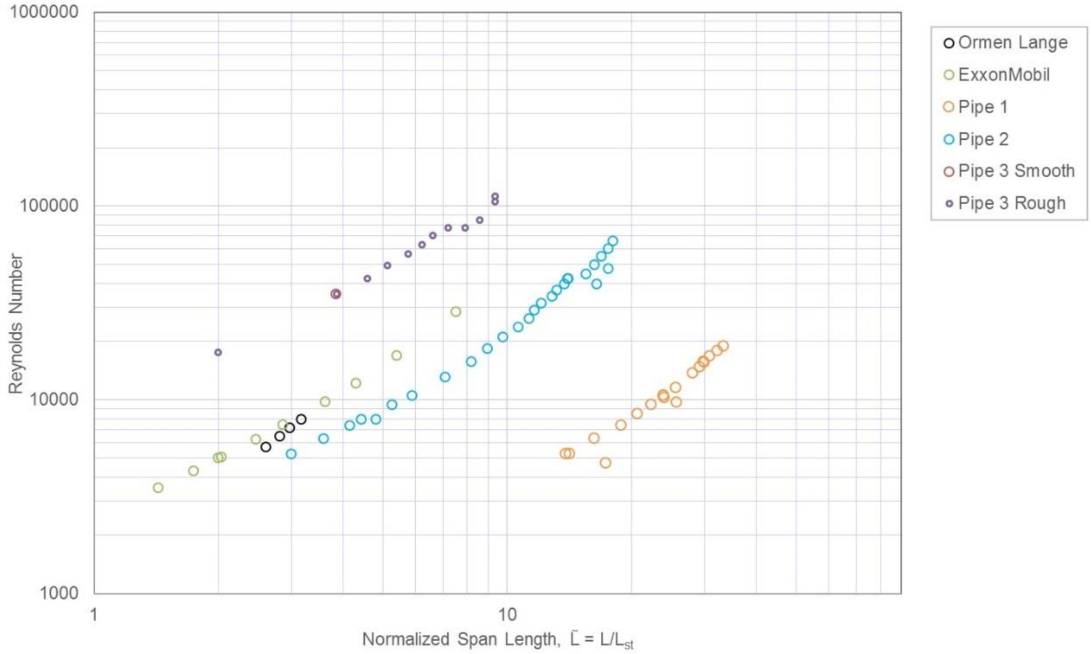

Figure 6.4 Reynolds numbers for included test data

Sponsor	Ormen Lange	Exxon Mobil	Shell		
			Pipe 1	Pipe 2	Pipe 3
Span Length, L (m)	11.413	9.63	38	38	38
Pipe Hydraulic Diameter, D (mm)	32.6	20	12	30	80
Length/Diameter Ratio, L/D	350	482	3167	1267	475
Mass Ratio, c_{pipe}	1.37	2.22	1.74	1.54	1.14
Maximum current velocity U tested (m/s)	0.28	2.24	3.45	2.51	1.60
Corresponding maximum test Reynolds Number (× 1000)	7.97	39.2	36.3	65.9	112.5
Axial Rigidity, EA (MN)	5.61	2.83	2.57	7.83	7.83
Flexural Rigidity, EI (Nm^2)	203	135.4	16.1	572.3	572.3
Stiffness of Axial Spring at one end, k_x (kN/m)	20.35	1.593	0.780	21	21
Factor by which axial flexibility is increased due to end spring, L_{ea}/L	25.1	185	87.6	10.8	10.8
Mass of clump weights at the ends of the model m_{clump} (kg)	none	none	500	500	500
Number of Tests included (those with $\psi_N \leq 0.1$ and $\psi_{arch,st} \leq 0.1$, a total of 99 tests)	4	10	19	27	13 (1 smooth + 12 rough)
Range of Normalized Span Lengths, $\tilde{L}$	2.6-3.2	1.4-7.5	14-33	3.0-18	2.0-9.3
Range of Normalized Effective Axial Force values, $\tilde{N}$	0.96-1.2	1.2-24	7.9-30	2.6-57	25-387
Range of calculated static rotations at ends (radians)	0.11-0.11	0.01-0.28	0.05-0.39	0.03-0.31	0.03-0.28
Range of Normalized fatigue-equivalent strain amplitudes, $\tilde{\epsilon}_e$, for cross flow direction above and in line below	4.3-6.1 3.4-4.7	3.5-5.4 2.5-5.5	6.4-13 7.0-13	6.1-11 4.4-9.7	8.7-13 7.4-12

Table 6.1 Model VIV test parameters and ranges of key reslts. The data shown are the same withing the test series corresponding to each column of the table.

6.2 Test Results

The results of the static solution of Appendix B are presented in Figure 6.5 and Figure 6.6. For these, the effective drag coefficient c_D is determined from the measured change in axial force arising from the flow. The drag coefficients thus obtained can only be accurate if this change in axial force is large compared to the axial force measurement error. Indeed, the calculation of c_d is not only affected by axial force measurement errors, but also by thermal expansion and any creep that occurs between the times of the two axial force measurements. For this reason, large errors can be expected when N/N_g is close to 1. Indeed, the data in Figure 6.5 are only complete for $N/N_g \geq 1.32$. For $1 < N/N_g < 1.32$ there are additional points ranging from $c_D = 0.56$ to $c_D = 18.1$ that fall outside the c_D range of the plot, and are judged to be unreliable. Further, the calculation of c_D is based on the assumption that it is constant along the length of the pipe, whereas in reality it may vary along the length of the pipe together with the amplitude of VIV.

The maximum normalized dynamic strain amplitudes $\tilde{\epsilon}$ are shown in Figure 6.7. More directly relevant to fatigue damage are the normalized fatigue-equivalent strains, $\tilde{\epsilon}_e$, which are calculated for the same locations where the dynamic amplitude of the bending strain is highest. These are shown in Figure 6.8 with $\tilde{L}$ values, and in Figure 6.9 with $\tilde{N}$ values. It can be seen that the fatigue-equivalent strains tend to be bit higher than the dynamic amplitudes. This is further illustrated by looking at the ratio of strains Figure 6.10: The fatigue-equivalent strain is up to a factor of 1.6 higher than that dynamic amplitude of the same strain, but for two of the EM tests, the fatigue-equivalent strain is below its dynamic amplitude. Therefore it is better to use fatigue-equivalent strains from VIV tests than dynamic amplitudes for fatigue assessments.

The scatter in Figure 6.8 and Figure 6.9, suggests that neither $\tilde{L}$ nor $\tilde{N}$ on its own is sufficient to predict the normalized fatigue-equivalent bending strain $\tilde{\epsilon}_e$. If the basic scaling assumptions hold, then $\tilde{\epsilon}_e=\tilde{\epsilon}_e(\tilde{L},\tilde{N},c_{pipe})$, i.e. the normalized equivalent bending strain is a function of the normalized span length, the normalized effective axial force, and the mass ratio. Assuming a linear relationship between the logarithms of these quantities yields the following optimized fits (in the sense that the sum of the squares of the logarithm of the ratio actual/predicted values is minimized):

$$\begin{aligned} \tilde{\epsilon}_e &= 4.90\ \tilde{L}^{0.152}\ \tilde{N}^{0.157}\ c_{pipe}^{-0.593} \quad \text{for cross flow} \\ \tilde{\epsilon}_e &= 2.72\ \tilde{L}^{0.215}\ \tilde{N}^{0.214}\ c_{pipe}^{-0.244} \quad \text{for in line} \end{aligned} \tag{25}$$

The ratio of actual/fitted value is plotted in Figure 6.11. Compared to Figure 6.8 and Figure 6.9 it is seen that this fitting reduces the scatter: The logarithmic standard deviations of the ratio of actual/fitted ratios are 0.16 and 0.17 for the cross flow and in line fits, respectively, compared with a logarithmic standard deviations for $\tilde{\epsilon}_e$ itself of 0.32 and 0.35, respectively. (The fitting ensures that the geometric average of the actual/fitted ratios is 1.)

Although, it is conceivable that by using a different functional form a better fit might be achieved, the nature of the remaining scatter in Figure 6.11 indicates otherwise. If a smooth function $\tilde{\epsilon}_e=\tilde{\epsilon}_e(\tilde{L},\tilde{N},c_{pipe})$ that fitted the data well existed, the test/predicted ratios in Figure 6.11 would also vary smoothly within each test program, much like the $\tilde{N}$ values vary smoothly with $\tilde{L}$ in Figure 6.3.

Considering only the data for which $(\tilde{L},\tilde{N})$ falls in the box shown in Figure 6.3, i.e., $(\tilde{L},\tilde{N}) \in [11,18.5] \times [5,10]$, there remains considerable scatter: the logarithmic standard deviations of the $\tilde{\epsilon}_e$ values in that box is 0.15 for cross flow, and 0.16 for in line, i.e. about the same as for the fit of Eq. (25). Further, in that box, 12 of the 13 data points are for Pipe 2, and only one for Pipe 1. I.e. almost all data come from the same pipe and test setup.

Efforts to refine the fitting further risk overfitting, especially considering that only 5 different pipes are involved, for each pipe essentially only the current velocity is varied, and the fits in Eq. (25) already involve 4 parameters adjusted to optimize the fit. For this reason, we rejected an attempt to also include the Reynolds number in the fitting process. It achieved a slightly closer fit, at the cost of the fitted $\tilde{\epsilon}_e$ decreasing with increasing Reynolds numbers, which is against the trend documented in [2,16]. Indeed, by considering 2 of the 5 test rigs considered here, the neural network fit in [16] also showed decreasing response with increasing Reynolds number, but after constraining their fit optimization so that the response increases with increasing Reynolds numbers, they suggest that "the cross-flow vibration amplitude was found to increase with Reynolds number in the same vibration mode but decrease suddenly as the vibration mode shifted to a higher number after which point it will continue to increase with Reynolds number until the next mode shift occurs." Here no attempt is made to achieve that sort or resolution with such limited data, and indeed the authors believe that additional complicating factors are likely at play, as alluded to in the discussion of scaling approximations in Appendix C.

There is no lack of possible explanations for the scatter in the data: that the function $\tilde{\epsilon}_e=\tilde{\epsilon}_e(\tilde{L},\tilde{N},c_{pipe})$ is not smooth, that one or more of the scaling assumptions are violated, or a combination of both. The accuracy of the scaling approximations is discussed in Appendix C. It remains that fatigue damage from VIV is difficult to predict, especially when several modes are excited, and testing limitations typically do not allow carrying out the tests at the desired Reynolds numbers.

To assess whether a much-used industry span assessment method might provide better predictions of fatigue damage than Eq. (25), each of the VIV tests is also analyzed according to F105 [3] as described in Appendix D, without using the safety factors in F105, but including arch action in the F105 calculation unless otherwise noted. Based on the fatigue damage rates calculated by F105, the corresponding normalized fatigue equivalent strains $\tilde{\epsilon}_e$ are calculated and the ratio of $\tilde{\epsilon}_e$ values from the test divided by those from F105 are plotted in Figure 6.12. Clearly F105 is not a good predictor of the fatigue-equivalent strain amplitude $\tilde{\epsilon}_e$. This is also reflected by the ranges shown in Table 6.2. They indicate that for in line, F105 is always conservative, but for cross flow, it may be non-conservative by up to a factor of 2.33 according to the selected available test data. The logarithmic standard deviations of the test/F105 ratio are 0.38 and 0.27, for cross flow and in line, respectively, are more than the 0.16 and 0.17, respectively, for the simple fit of Eq. (25). Even using $\tilde{\epsilon}_e$ = 7.66 for cross flow irrespective of test conditions more accurately predicts the test data than F105 with a logarithmic standard deviation of 0.32 instead of the 0.38 for F105. Of course, although using F105 for high-mode response (i.e. high $\tilde{L}$ values) is "allowed", F105 has not been developed for truly high mode response. The multi-mode formulations in F105 are calibrated on the Ormen Lange data some of which are included here. Indeed, for the selected Ormen Lange Data, the logarithmic standard deviation of the test/F105 ratio of fatigue-equivalent strains is only 0.14 for cross flow and 0.13 for in line, as per the last row of Table 6.2. For higher $\tilde{L}$ values, F105 is seen to be more conservative, perhaps to cover the uncertainty arising from limited calibration effort in that domain.

Test / F105 Fatigue-Equivalent Strain Ratio Statistic	Cross Flow	In Line
Maximum Value	0.36	0.27
Minimum Value	2.33	0.96
Geometric Mean Value	0.78	0.48
Standard Deviation of the Natural Logarithm ("Logarithmic Standard Deviation")	0.38	0.27
Geometric Mean Value for Ormen Lange Data only	1.01	0.83
Logarithmic Standard Deviation for Ormen Lange Data only	0.14	0.13

Table 6.2 Statistics for ratio of fatigue-equivalent strain amplitude from test divided by that calculated by F105 without safety factors, based on included cases (as defined in Section 6.1) with arch action included in the F105 calculation

Wherever the test/F105 ratios are presented, arch action has been included in the F105 prediction. However, it does not make much difference if arch action is included or not, since limited arch action is one of the criteria for test data selection in Section 6.1. Specifically due to arch action, the geometric mean value of the actual/F105 ratio of $\tilde{\epsilon}_e$ values increases by 0.79% for cross flow and decreases by 0.02% for in line, and the logarithmic standard deviation decreases by 0.33% for cross flow and by 0.06% for in line. (Arch action affects the in line as well as the cross flow directions, since under the steady state force from the current, the pipe hangs in an inclined "static plane", as explained in Appendix B and D.)

Further remarks in regard to F105 are:

1) If the structural model used in the F105 calculations satisfies the basic structural scaling approximations, it will produce the same results when applied to the model or the prototype provided that $\tilde{L}$, $\tilde{N}$, and c_{pipe} is the same. The scaling result that $\tilde{\epsilon}_e$ only depends on $\tilde{L}$, $\tilde{N}$, and c_{pipe} also applies to the F105 calculation.
2) Further to the above, the sensitivity of the F105 calculation to c_{pipe} is small, as it only affects certain calculated oscillation frequencies used for fatigue cycle counting only and not the amplitudes of displacement and strain.

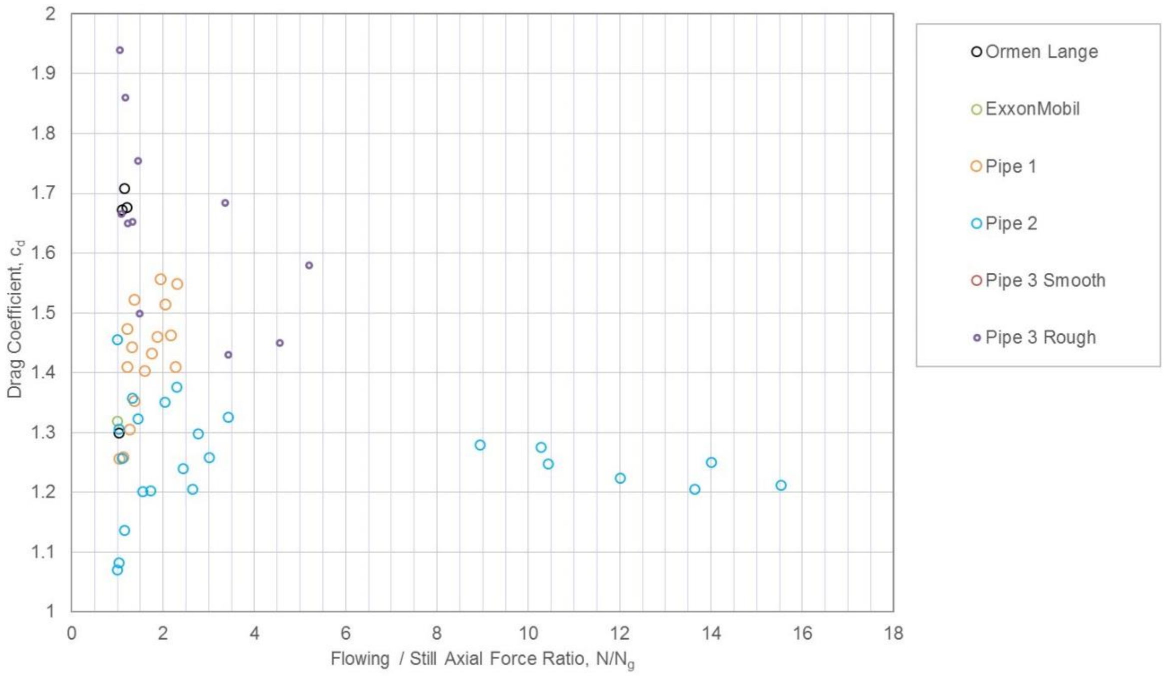

Figure 6.5 Drag coefficients calculated from the change in axial force from N_g under gravity only to N, the static component under flowing conditions.

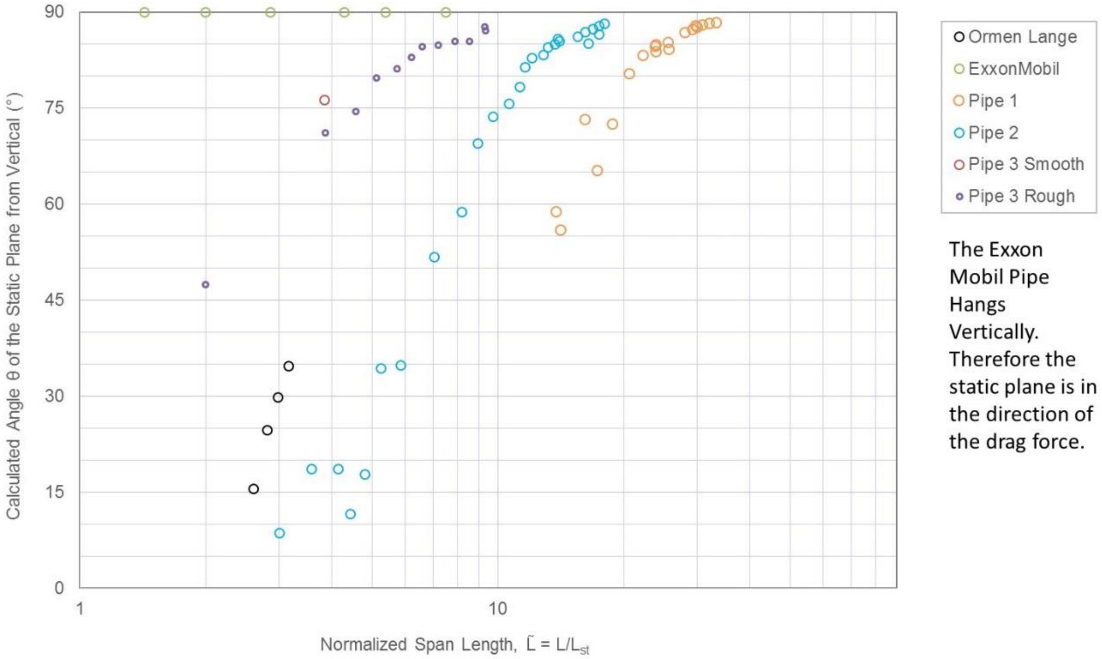

Figure 6.6 Inclination θ of the static plan plane in which the pipe hangs under the action of gravity and a drag force that is assumed to be constant along the length of the pipe. θ = 0° means the pipe hangs vertically with negligible drag whereas θ → 90° means it hangs horizontally under the drag force which must be very large compared to the gravity force. Where arch action is significant, the vibration modes are in the static plane and normal to it, rather than in line and cross flow. See Appendix B.

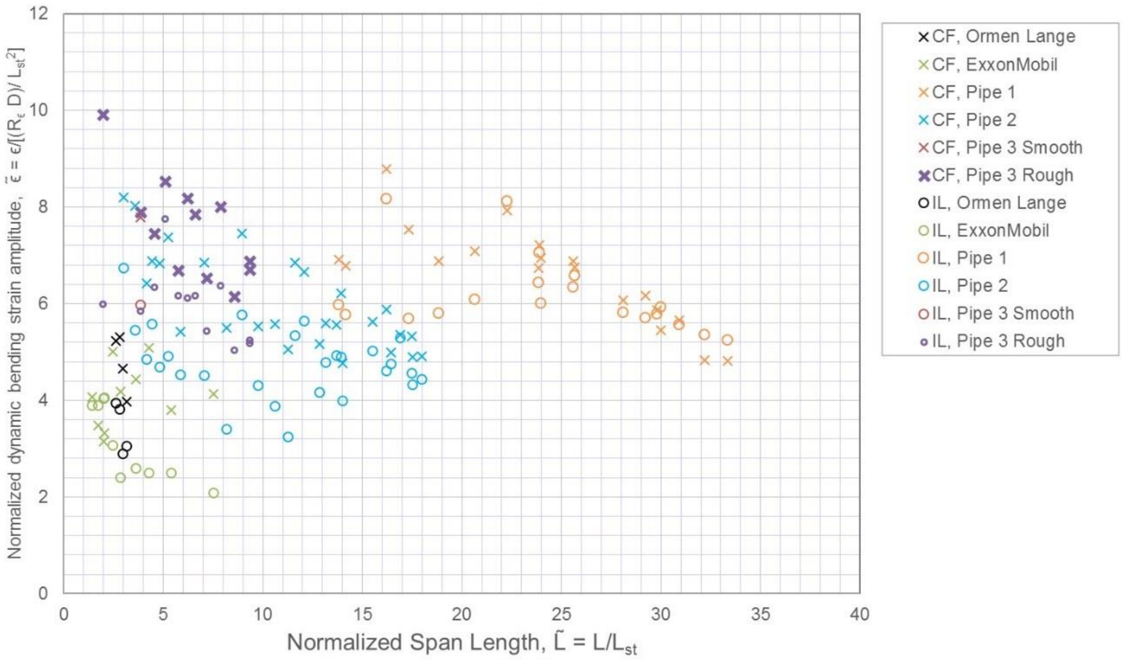

Figure 6.7 **Maximum values of the normalized dynamic bending strain amplitude**

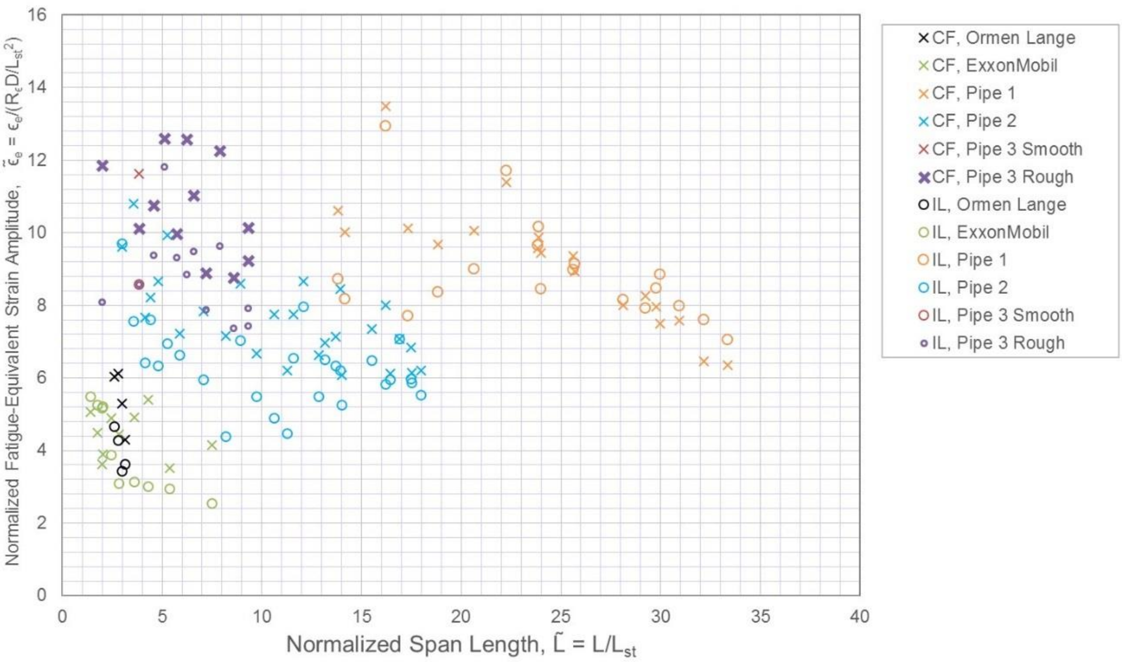

Figure 6.8 **Normalized fatigue-equivalent bending strain amplitudes calculated for the locations where the dynamic bending strain amplitude is highest, shown as a function of $\tilde{L}$**

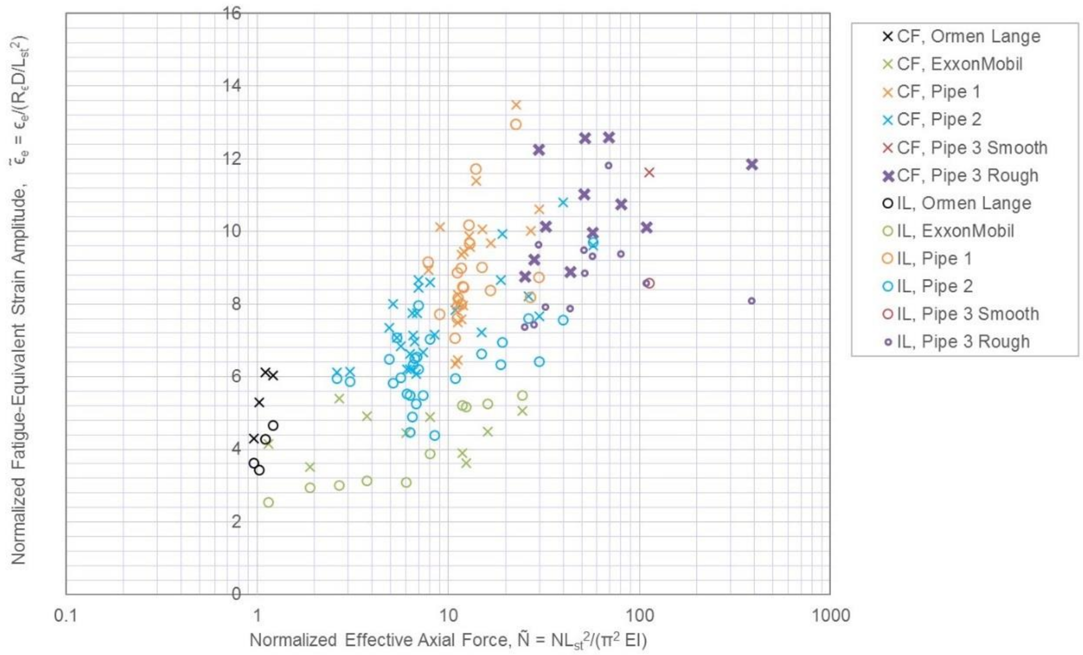

Figure 6.9 Normalized fatigue-equivalent bending strain amplitudes calculated for the locations where the dynamic bending strain amplitude is highest, shown as a function of Ñ

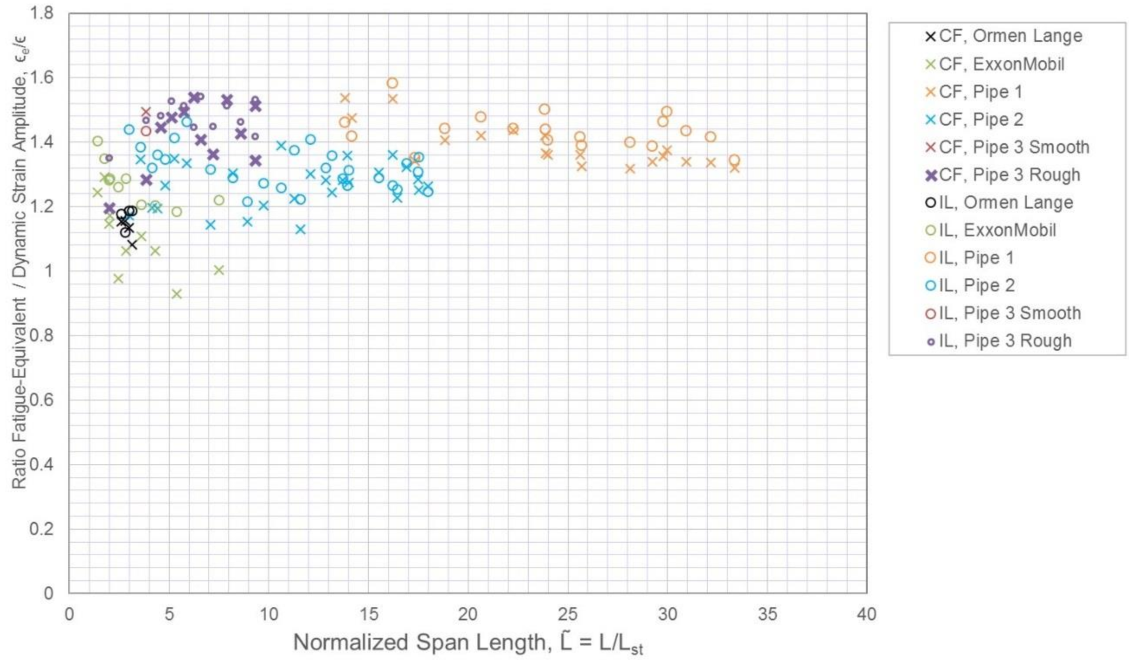

Figure 6.10 Ratio fatigue-equivalent / dynamic amplitudes for the bending strains at the locations where the dynamic amplitude is highest

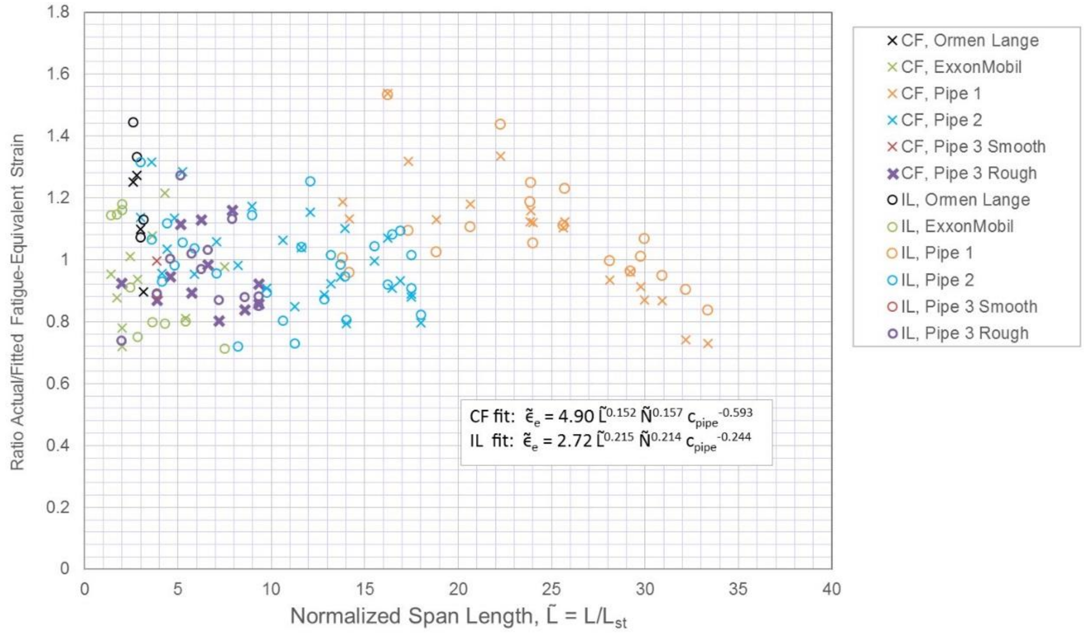

Figure 6.11 Ratio of actual/fitted values of the (normalized) fatigue-equivalent bending strain based on the fit from Eqs. (25)

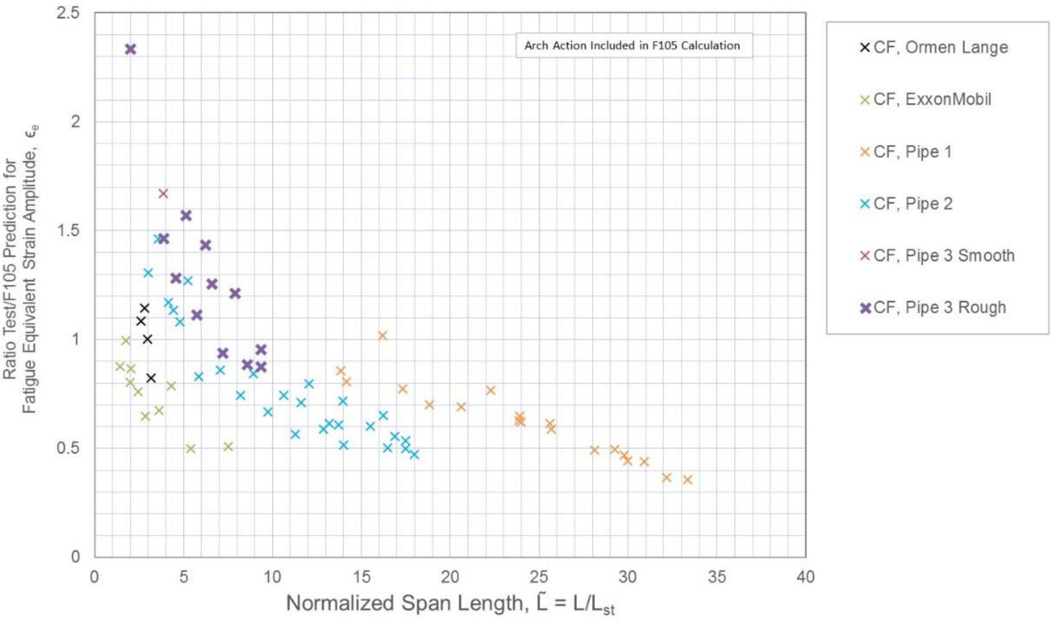

Figure 6.12 Ratio of the normalized fatigue-equivalent bending strain from the VIV tests divided by that calculated by applying F105 [3] with arch action as described in Appendix D.

7 Structural Damping

The VIV test models [19,22,23] were designed to ensure low structural damping. In view of this and the great uncertainty about the structural damping for the modes, frequencies and amplitudes excited, the structural damping has not been included in the analysis of the test data.

Structural damping tests have been performed in air, since even in still water hydrodynamic damping is significant. The pipe is manually excited at the quarter point (25% of the span length from one end), and the decay in response after the excitation ceases is used to estimate the damping ratio.

Thus, for the OL tests, around 0.4% damping is measured for Modes 1 to 3; for the EM tests, “the structural damping was measured to be less than 0.3% of critical” [19]. For the Shell-sponsored tests on Pipes 1 to 3, structural damping values are not reported in [23], but [13] does report an “average” structural damping ratio of 0.5% for Pipe 1.

For Pipes 2 and 3, re-examining the acceleration records during the damping tests, filtered to include the frequency range 1 to 5 Hz only, and double integrated to convert accelerations to displacements yielded the following: For Pipe 2 the damping ratios range from 0.6% to 0.8% for Mode 2 at amplitudes ranging from 5.1 D to 2.9 D. For Pipe 3, 1.5% damping is obtained at amplitudes ranging from 2.8 D to 0.7 D. Modes 2 and 3 were excited which resulted in some beating in the response, which made it more difficult to accurately estimate damping from the decay in amplitude of free vibrations. It is thought that the higher damping for Pipe 3 compared to Pipe 2 may be due to the half shells used to increase the hydrodynamic diameter of the pipe.

All these damping tests involve low modes, whereas the VIV response often involved much higher modes. ($\tilde{L}$ is essentially the mode number that is excited at the Strouhal frequency.) Thus, there is great uncertainty about the actual structural damping for the modes, amplitudes, and frequencies of VIV, as noted in [13].

Although models typically include viscous damping, for which the damping force is proportional to the velocity, the damping could also be hysteretic (with a magnitude of the damping force that does not change with velocity), or quadratic. This affects how the energy dissipated per cycle varies with amplitude and frequency. E.g., (Coulomb) frictional dissipation is more likely to give rise to hysteretic damping for which the energy dissipated does not change with frequency and is proportional to the amplitude itself, whereas for viscous damping the dissipated energy per cycle is proportional to frequency and amplitude squared.

Moreover, the damping mechanism is unclear. In [13] the structural damping is modeled in the same way as hydrodynamic damping, by distributed dashpots applying a transverse force on the pipe that opposes the transverse component of pipe velocity. This may be realistic for soil damping where the pipe is supported by the soil, but not for the structural damping of the model tests. A more reasonable approach is to include structural damping where there is structural stiffness.

Three categories of structural stiffness and the associated damping can be distinguished: (1) that associated with arch action, (2) that associated with the axial tension without arch action , and (3) that associated with flexural resistance. The first could be important, for low modes, e.g. affecting the measured damping value for Mode 1, but since the higher modes are hardly affected by arch action, the same will apply to any damping associated with arch action (i.e. damping in the axial deformations of the pipe, in the spring that maintains the tension, and in any of the associated connections and hinges). The second is zero at amplitudes sufficiently small that the linearized theory applies [14]. Only the last has been included in the formulation (Eq. (5)).

Structural nonlinearities can also affect energy dissipation, e.g. by changing the frequency of part of the kinetic energy to one that is more strongly damped.

Assuming that the measured damping ratios are due to flexural, viscous damping, the damping coefficient C_k can be calculated, and used to calculate the normalized damping values $\tilde{C}_k$ for each VIV test. However, this gives normalized damping values $\tilde{C}_k$ that are far too high for some of the VIV tests. Thus, flexural viscous damping cannot be the only source of damping in the damping tests. Assuming flexural hysteretic damping would lead to much lower $\tilde{C}_k$ values. In theory, whether the damping is viscous or hysteretic could be determined from be determined from how the decay rate of the vibrations during the damping tests depends on the amplitude, but re-processing the damping test acceleration records for Pipes 2 and 3 did not reveal a clear amplitude dependence of the decay rate.

Thus, there remains a large uncertainty about the amount of damping present in the VIV tests, but it is not expected that the structural damping is sufficiently high to have a large effect of on cross-flow VIV. Nevertheless, it is conceivable that for the extremely high-mode response of Pipe 1 in Figure 6.8, the downward trend with increasing $\tilde{L}$ for $\tilde{L} > 20$ may in part be due to structural damping, possibly associated with geometric nonlinearity for such high-mode response.

The authors fully concur with the recommendation in [13] that more attention should be focused on understanding and quantifying the structural damping of VIV test models for the modes excited by the VIV. For instance, if necessary by also performing damping tests on shorter span models, and performing tests with accurately-controlled harmonic excitation as well as free vibration decay tests.

8 Prototype Example

8.1 Prototype Definition

Here "prototype" refers to a pipeline span to be assessed. For the example considered, the span length is L=150m; the steel pipe outer diameter is 24inches (0.6096m); the wall thickness of steel is 17mm, the corrosion coating has a thickness of 6mm and density of 1300kg/m^3, outer concrete weight coating thickness is 40mm with a density (including water absorption) of 2400kg/m^3, the steel has Young's modulus of 207GPa, and a density of 7850kg/m^3, and the densities of the gas inside the pipeline and the seawater outside are 100kg/m^3 and 1025kg/m^3, respectively. The stiffness of the coatings is neglected. The mass ratio for the pipe is thus calculated to be $c_{pipe} = 1.234$.

To match the model tests, the ends are assumed to be simply supported, and the level of axial restraint is determined by assuming linear distributed axial soil springs with a stiffness of 5MN/m^2, which implies $L_{ea} = 2268$m, and an equivalent axial spring stiffness at one end of the span of $k_x = 90.5$ MN/m. (Use of the equivalent end spring allows the same formulation given in Appendix B for arch action to be used for this prototype span as it is for the model spans.)

The effective axial force under still-water conditions is assumed to be 1MN. However, this axial force increases with the flow, as determined by the static solution of Appendix B using a drag coefficient of $c_d = 1.5$. (An alternative might be to use the drag coefficients from Figure 6.5 determined for the model tests from the measured change in axial force due to the flow. Those account for the increase in drag due to VIV, but may suffer inaccuracies e.g. due to force measurement errors, unrecorded thermal expansion, or creep, especially where the increase in axial force due to the flow is small.)

For the fatigue resistance, the API X' curve is used for which the exponent is n = 3.74, and $a_{fat} = 6.89 \times 10^{35}$ Pa^n. (The same value of the exponent is used for the model tests to evaluate the normalized fatigue-equivalent strains, as it should be. The value of a_{fat} is not needed to calculate any of the parameters reported for the model tests, but it is needed to report the actual fatigue damage rates for the prototype.)

The above bears some similarity to a span assessed by some of the authors in which the pipe crossed a shallow channel. For a limited time, a turbidity current ("TC") travelling down channel can reach high current velocities. The lateral displacements it produces increases the axial tension and thus the span length. However, the example here has been much simplified, to focus on issues that can be captured by the model tests, enable the use of the analytical solution of Appendix B, and ensure easy reproducibility of the results. Phenomena for the real span under TC loading that are not modelled include: pipe soil interaction at the shoulders, including nonlinearity loss of contact and energy dissipation, nonlinearity and history dependence in the axial resistance at the shoulders, and the increase in span length with increasing current velocities and axial forces. Although, these phenomena are certainly important, and the scaling theory presented here could be used to design model tests to address them, they are beyond the scope of this paper.

8.2 Dominant Half Wavelength, λ

To apply scaling Assumption (9), the dominant half wavelength, λ, is needed. This is done in different ways according that what data are collected for the tests: For the Shell tests (Pipes 1 to 3) acceleration data collected at 22 points along the span are used to perform Fourier analysis. For the other data a dominant mode number, $n_{dominant}$, is estimated by inspecting the data (using engineering judgment), and the dominant wavelength is then calculated from $\lambda = L/n_{dominant}$. The resulting dominant wavelengths are shown in Figure 8.1 in normalized form as $\tilde{\lambda} = \lambda/L_{st}$.

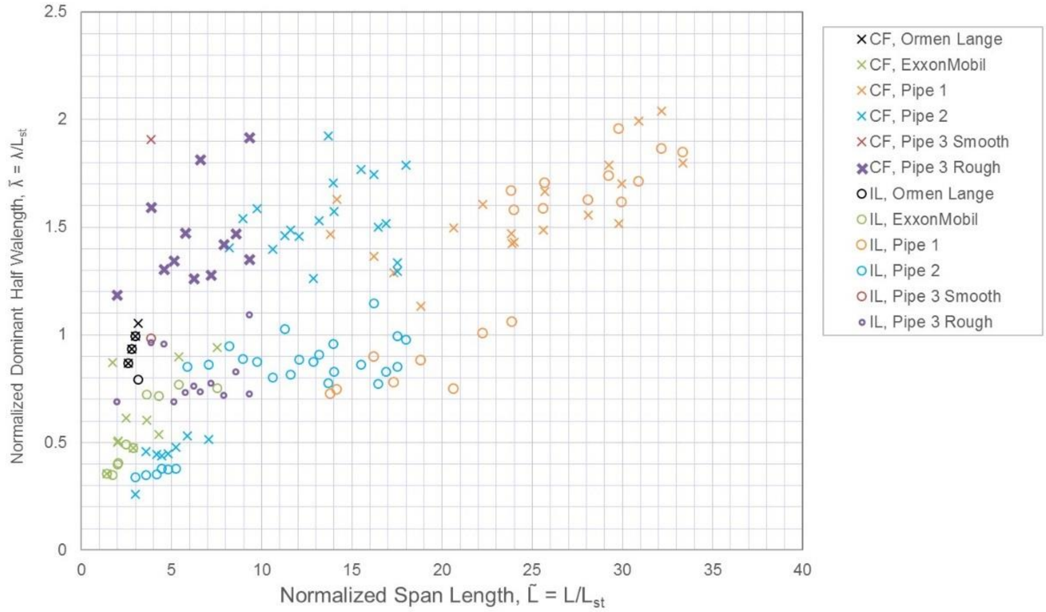

Figure 8.1 Normalized dominant half wavelengths, $\tilde{\lambda} = \lambda/L$ for model tests

8.3 Scaling Results

First the static solution is calculated, this then provides the required inputs for scaling the dynamic response from the model tests. The former is done analytically, with the result from Appendix B. For that purpose it is easiest to assume a value of the axial force N under flowing conditions, and then determine the current velocity U_c at which that axial force is reached. The resulting static solution is shown in Figure 8.2 to Figure 8.4.

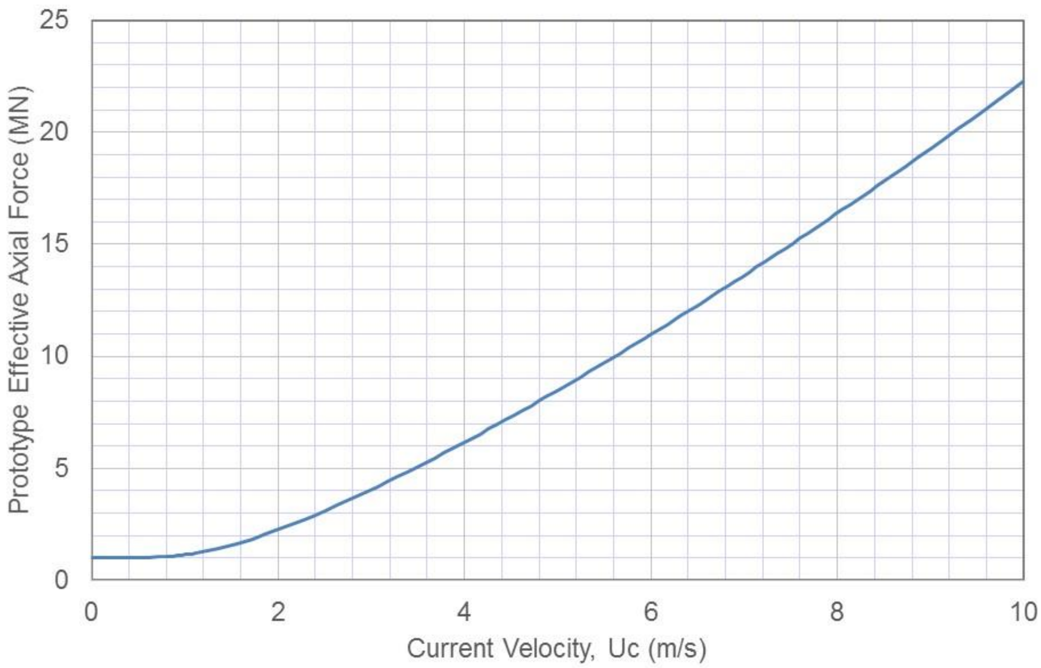

Figure 8.2 Effective axial force from static solution for prototype span

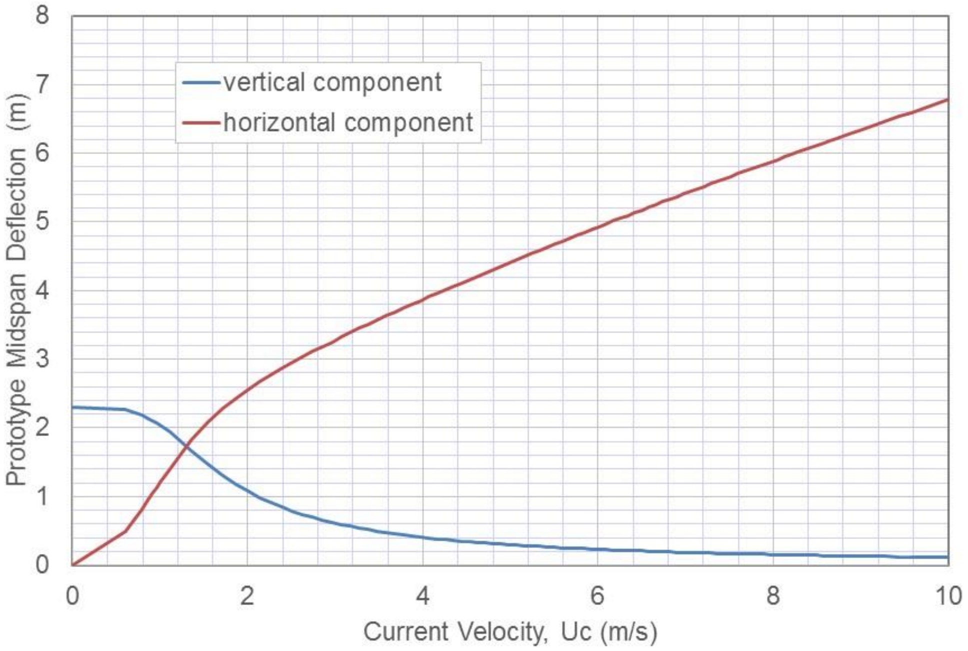

Figure 8.3 Midspan deflections from static solution for prototype span

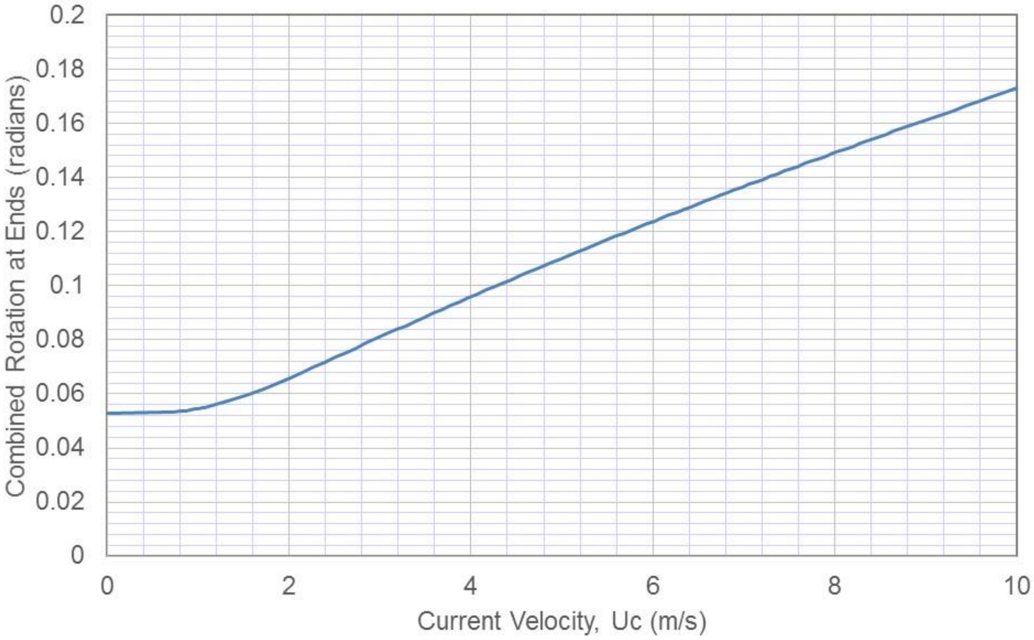

Figure 8.4 End rotations (in radians) from static solution for prototype span, combined rotation from gravity and hydrodynamic drag force.

The scaling results are applied to the dynamic part of the response, using the extended scaling approximations of Section 5 as well as the basic assumptions of Section 2. Thus, for every model test, a prototype current velocity is determined for which similarity is satisfied. The steps involved are as follows:

1) Start with an assumed axial force N and calculate the corresponding static solution including the prototype current velocity U using the static solution of Appendix B.
2) Determine the dominant half wavelength λ and the Strouhal length L_{st} for the prototype by applying the scale factor (i.e. prototype/model ratio of span lengths) to the model values.
3) Calculate adjusted values of the flexural rigidity and effective axial force for the prototype, EI_{adj} and N_{adj} from Eqs. (20) and (21), using the model values for the normalized quantities, and the prototype values otherwise.

4) Repeat the above steps updating the assumed N in Step 1 until Eq. (8) is satisfied with the adjusted values of EI and N, and with T_{st} calculated for the prototype using Eq. (7). From the static solution this then also gives the prototype current velocity U for which similarity with the model test is satisfied. Here the solution is sought for prototype axial forces in the range 1.0000000001MN to 22.28MN, corresponding to prototype current velocities in the range 0.005m/s to 10m/s. If no solution is found in that range, the model test is considered not relevant. For such cases it may represent even higher current velocities, but the axial force corresponding to 10m/s current velocity is already more than the pipe could sustain without yielding.
5) Any parameters of interest may now be calculated by multiplying the normalized values from the model test by the unit value for the prototype. For instance the unit value for the fatigue damage rate are calculated with Eqs. (17) and (14), which may be combined to yield $\dot{\eta}_1=[R_\epsilon D/(L_{st}^2\epsilon_{fr})]^n/T_{st}$, or, if the fatigue resistance is characterized by a_{fat} rather than ϵ_{fr}, $\dot{\eta}_1=[E R_\epsilon D/L_{st}^2]^n/(a_{fat}T_{st})$. The fatigue damage rate then becomes $\dot{\eta} = \dot{\tilde{\eta}}\, \dot{\eta}_1 = (2\tilde{\epsilon}_e)^n\, \dot{\eta}_1 = [2\tilde{\epsilon}_e E R_\epsilon D/L_{st}^2]^n/(a_{fat}T_{st})$. These fatigue damage rates are plotted in Figure 8.5 for the relevant model tests together with the relevant current velocity.

The above algorithm can easily be adapted if the static solution is determined by FE analysis rather than analytically. The FE analysis is then performed for increasing values of the current velocity, until conditions are such that Eq. (8) is satisfied, as in Step 4 of the above algorithm. The static FE analysis may then include any desired nonlinearities, including changes in span length, L.

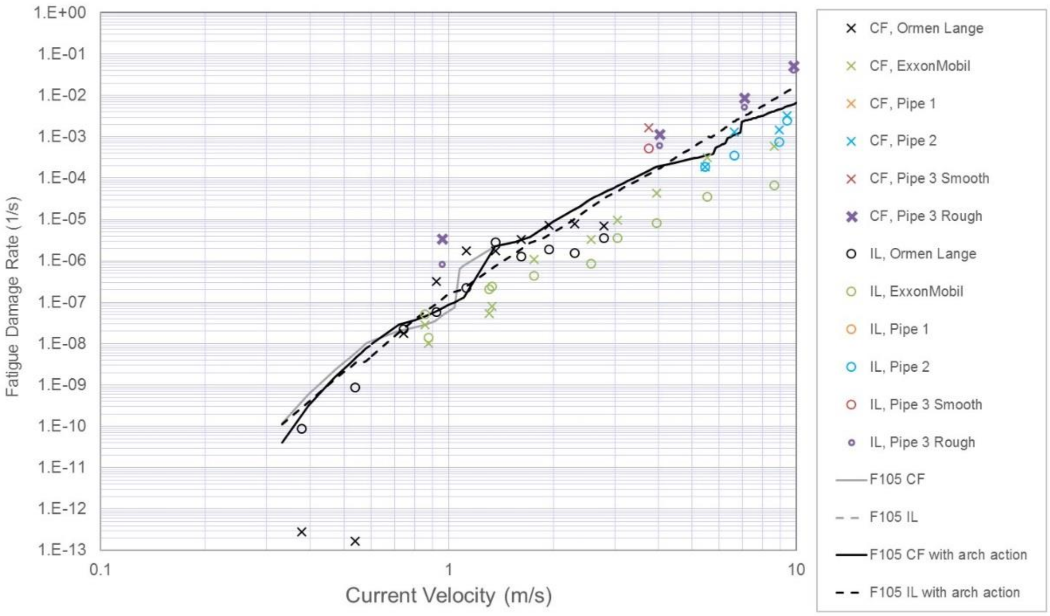

Figure 8.5 Prototype fatigue damage rates as a function of current velocity from scaling of model tests, and by applying F105 [3] with and without considering arch action in the modal analysis

8.4 Predictions from DNVGL Recommended Practice F105

For comparison with the scaled model test results, the predictions from F105 [3] are also included in Figure 8.5. For that purpose the modes are calculated with and without including arch action, using the analytical solution of Appendix B. Further details needed in addition to [3] to make the F105 calculation results reproducible are given in Appendix D.

For low current velocity, F105 predicts zero response and fatigue damage rate, which is not included in Figure 8.5, because it would be off the logarithmic scale used.

8.5 Vivana Analyses

For comparison the prototype pipe is also analyzed with the frequency-domain version of Vivana [4]. The structural model in VIVANA consists of 300 elements of equal length. Both ends are pinned except for that the pipe is free to extend in the axial direction at one end, where an axial force is applied that is a function of the current velocity only, as given in Figure 8.2. Thus, arch action is neglected. The default hydrodynamic lift and mass coefficients are used, which are generalized based on laboratory test data [4]. The drag coefficient is taken to be 1.5, as for the F105 analyses. The Vivana static lateral and vertical deflections are indistinguishable on a plot from those in Figure 8.3. Pure CF analysis yields the fatigue damage rates included in Figure 8.5. Although the Vivana CF fatigue damage rates tend to increase with current velocity, as expected, this increase is not monotonic. The sudden drops appear to be associated with mode shifts, i.e., the responses reduce before the next mode can be fully excited.

8.6 Partial Strake Coverage

Some tests on Pipe 3 include strakes with a gap in the strake coverage centered at midspan. E.g. the span is "75% straked" if the gap in the strake coverage at midspan is 25% of the span length. The strakes are described in [23]: they have a height of $0.25D_h$ and a pitch of $15D_h$, with 3 starts so that there is one strake at every 120° of the circumference. Here $D_h = 1.075$ D is the hub diameter, i.e. diameter of the pipe from which the strake fins protrude. (For Pipe 3 the outer diameter of the bare pipe is D=80mm, but adding the half shells with strakes the hub diameter is D_h=86mm.) The analysis to determine the fatigue damage rate from the model tests for a prototype with similar strake coverage is the same as for the bare pipe (as per Section 4), except that the effect of the strakes on the drag coefficient should be considered in calculating the static solution for the prototype. The strakes tend to increase the drag, but so does VIV which mainly occurs when no strakes are present. For simplicity the same drag coefficient of 1.5 for the bare prototype is also used for the straked parts of the prototype. This is close to the drag coefficients of around 1.4 reported in [24] for pipes with similar strakes, except that the pitch of the strakes in [24] is 17.5 D instead of 15 D. (An alternative is to use the effective drag coefficients determined indirectly, as in Appendix B, from the VIV tests on the straked pipe, assuming the drag coefficient is constant along the length of the pipe.)

The resulting cross flow fatigue damage rates for the prototype straked pipe are shown in Figure 8.6. As expected, the strakes bring about a large reduction in fatigue damage rate, though some of the 48% straked Pipe 3 tests show a higher fatigue damage rate than EM tests on bare pipe corresponding similar prototype current velocities. The in line fatigue damage rates for the partially straked pipes are not shown in the figure, but are all lower than the corresponding cross flow ones.

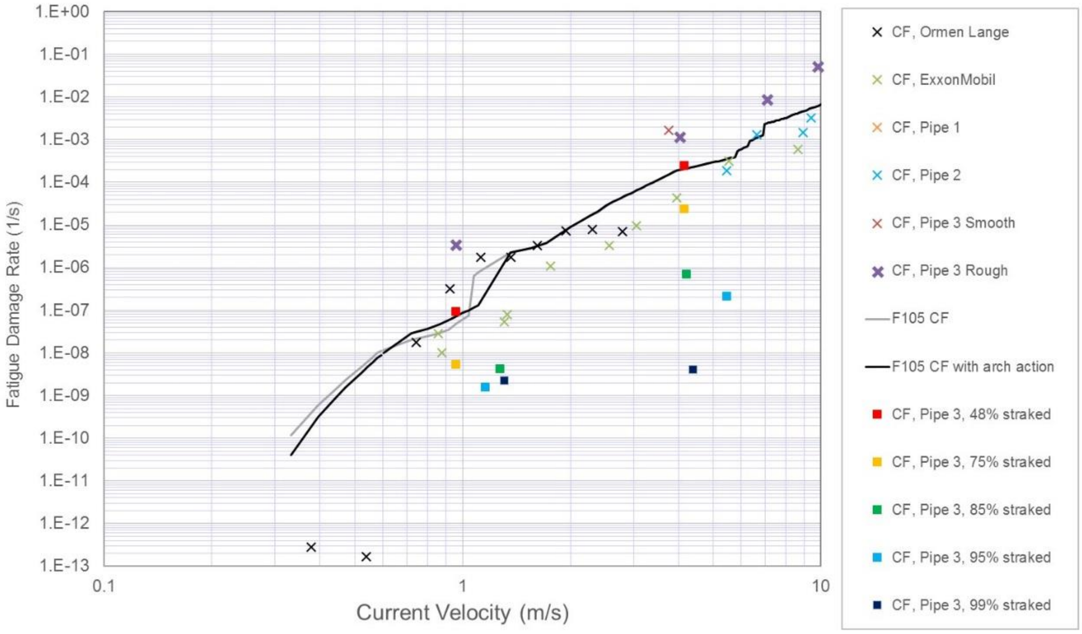

Figure 8.6 Prototype cross flow fatigue damage rates for partially strake covered pipe shown as solid squares together with the cross flow data for bare pipe from Figure 8.5

8.7 Discussion of Prototype Results

If all scaling approximations are good, the scaled experimental results in Figure 8.5 should coalesce into a single line. That relies on the extended as well as the basic scaling approximations. Clearly the scatter about this "single line" is large. To quantify the scatter, the F105 predictions are used as a reference line that reasonably captures the velocity dependence of the fatigue damage rate. Considering the data in Figure 8.5 for current velocities in the range 0.6 to 10m/s, the scaled/F105 ratio of fatigue damage rates range from 0.0408 to 47.7, with a geometric mean value of 0.72 and a logarithmic standard deviation of 1.80. For in line, this scaled/F105 ratio of fatigue damage rates ranges from 0.0376 to 6.78, with a geometric mean value of 0.35, and a logarithmic standard deviation of 1.54. It is not clear that causes this high scatter in results, but, whatever it is, is not captured by the F105 analysis.

Neglecting the mass ratio c_{pipe} (as per extended scaling Approximation (8)) could well be responsible for the relatively low fatigue damage rates for the ExxonMobil ("EM") tests, with $c_{pipe} = 2.22$, compared to Pipe 3 with $c_{pipe} = 1.14$. These correspond to the highest and lowest values of c_{pipe}, respectively; see Table 6.1 for the mass ratios of the other tests. Other test data that show a similar trend with respect to the mass ratio, include the 1 or 2 degree of freedom tests of a rigid cylinder supported by springs in [18], which cover a very wide range of mass ratios. There the mass ratio hardly affects the peak response, but it has much more effect on the range of current velocities over which high response occurs. In the multi-mode case, this could translate to more modes responding simultaneously.

Adjusting N and EI to match the model $\tilde{N}$ values as per Eqs. (20) and (21) achieves the correct structural stiffness to resist pipe out of straightness at the dominant wavelength, but not at other wavelengths. To assess the error of the approximation, the stiffness at half the dominant wavelength is considered. In particular, the ratio of this stiffness after the adjustment divided by that before the adjustment is plotted in Figure 8.7. It ranges from 0.56 to 1.4. There is no apparent correlation between the scatter in Figure 8.5 and this stiffness ratio. This does not necessarily mean that the error due to adjustment of EI and N is insignificant, but the test data used appears insufficient to quantify what it may be.

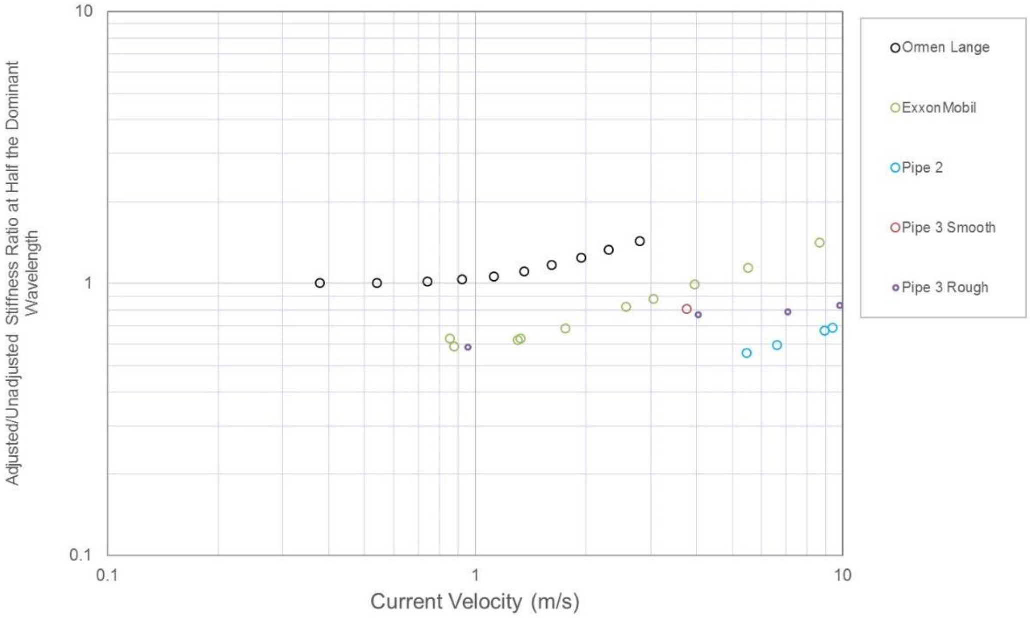

Figure 8.7 Ratio of structural stiffnesses to resist out-of-straightness at half the dominant wavelength divided by the unadjusted value

9 Conclusions

Advantages of the scaling developed include:

1) The number of dimensionless parameters is reduced by scaling assumptions that serve as approximations. These include local action by which D/L need not match, and using the Von Kármán beam theory for moderately large deflections with constant axial force to reduce the number of parameters required for the "complete" [10] structural characterization of the span.

2) Using the Strouhal period T_{st} and half wavelength L_{st} as the units of time and length in the axial direction, and the hydraulic diameter D as the unit of length in the transverse direction makes the normalized parameters physically meaningful. It also makes it clear how to extend the scaling, e.g. to include a soil-supported part of the pipe.
3) The normalized parameters are stable; they do not vary widely with the normalized VIV test design parameters.
4) The normalized fatigue-equivalent strain amplitude $\tilde{\epsilon}_e$ is not only stable, but also gives the fatigue damage rate directly, based on the rainflow counting performed for the test data.

The basic scaling approximations applied to a simply supported structurally undamped pipe lead to $\tilde{\epsilon}_e=\tilde{\epsilon}_e(\tilde{L},\tilde{N},c_{pipe})$. I.e. that the normalized fatigue-equivalent bending strain is a function of the normalized span length, the normalized effective axial force, and the mass ratio.

Further, extended scaling approximations in principle allow any VIV test to be scaled to any prototype, provided the end conditions are similar (e.g. both simply supported), and the model and protype current velocities are related for similarity.

To assess a prototype span, the static equilibrium configuration is determined by analysis. This completes the input to the scaling of the dynamic response.

This scaling is applied to VIV test data from well-instrumented tests from three testing programs carried out at Marintek (currently SINTEF Ocean). The data do not allow a direct experimental verification of the scaling approximations, because there are no two tests on different pipes for which the normalized input parameters $(\tilde{L},\tilde{N},c_{pipe})$ are the same. However, the data do allow comparisons of different test programs, and provide data points for estimating the function $\tilde{\epsilon}_e=\tilde{\epsilon}_e(\tilde{L},\tilde{N},c_{pipe})$ for essentially undamped, simply-supported spans.

The scatter in the results suggest that either the function $\tilde{\epsilon}_e=\tilde{\epsilon}_e(\tilde{L},\tilde{N},c_{pipe})$ is not smooth, or inaccuracies in the scaling approximations are considerable. The latter are assessed (in Appendix C) using relative error indicators denoted by ψ, and the data used have been selected to exclude those for which larger scaling errors are incurred.

Where clump weights have been used to stabilize the ends of the test pipe, axial modes at around the frequency of VIV response may be excited by geometrically nonlinear affects, including those that are nonlinear in the dynamic increment, and those termed “arch action” arising from the static loads (i.e. that the static loads change the behavior for small superposed increments).

10 Acknowledgements

The authors are grateful for permission to use the data from tests sponsored by ExxonMobil, Shell, and the Ormen Lange License Holders (Petoro AS, Equinor Energy AS, A/S Norske Shell, PGNiG Upstream Norway AS, and Vår Energi ASA). This research did not receive any specific grant from funding agencies in the public, commercial, or not-for-profit sectors.

11 References

1. Sarpkaya, T. (1979), "Vortex-induced oscillations: A selective review", Journal of Applied Mechanics, 46 (2): 241–258.
2. Swithenbank, S.B., Vandiver, J.K., Larsen, C.M., Lie, H. (2008) “Reynolds Number Dependence of Flexible Cylinder VIV Response Data,” Proc. of the ASME 27th International Conference on Offshore Mechanics and Arctic Engineering, June 15-20, 2008, Estoril, Portugal, Paper No. OMAE2008-57045.
3. Det Norske Veritas (2017), "Free Spanning of Pipelines," Recommended Practice DNVGL-RP-F105, June 2017.
4. SINTEF Ocean (2019) "VIVANA 4.16.2 Theory Manual", Tronhdeim, Norway.
5. Triantafyllou, G.S. (1998) "Vortex induced vibrations of long cylindrical structures," Paper presented at the 1998 Summer Meeting of the American Society of Mechanical Engineers, Washington, D.C.
6. Zheng, H., Price, R., Modarres, Y., Triantafyllou, G.S. and Triantafyllou, M.S. (2011) Vortex induced vibration an analysis (VIVA) based on hydrodynamic databases Proceedings of the 30th

International Conference on Offshore Mechanics and Arctic Engineering, OMAE 2010, Rotterdam, The Netherlands, June 19 - 24, 2011, Paper No. OMAE2011-50192.
7. Fontaine, E., et al. (2011) “Reliability based factors of safety for VIV fatigue using NDP riser high mode VIV tests,” Proceedings of the ASME 2011 30th International Conference on Ocean, Offshore and Arctic Engineering, OMAE2011, July 19-24, 2011, Rotterdam, The Netherlands, Paper No. OMAE2011-49820.
8. Yang, G., Frank, W.R., Campbell, R.B. and Slocum, S.T. (2008) “VIV Model Test Data Comparison with SHEAR7 V4.5,” Proceedings of the ASME 27th International Conference on Offshore Mechanics and Arctic Engineering, OMAE2008, June 15-20, 2008, Estoril, Portugal, Paper No. OMAE2008-57108.
9. Pontaza, J.P., and Menon, R.G., (2013), "Prediction of Vortex-Induced Vibration Response of a Pipeline Span by Coupling a Viscous Flow Solver and a Beam Finite Element Solver, " Published in Journal of Offshore Mechanics and Arctic Engineering. August 2013, Vol. 135 Issue 3, p31702, 9 p.
10. Buckingham, E. (1914) “On physically similar systems; illustrations of the use of dimensional equations,” Physical Review 4 (4), 345-376.
11. Buckingham, E. (1915). “Model experiments and the forms of empirical equations,” Transactions of the American Society of Mechanical Engineers, 37: 263–296.
12. Gao, Y., Fu, S., Wang, J., Song, L. and Chen, Y. (2015) "Experimental study of the effects of surface roughness on the vortex-induced vibration response of a flexible cylinder," Ocean Engineering103(2015)40–54.
13. Vandiver, J.K., Ma, L. and Rao, Z. (2018) "Revealing the effects of damping on the flow-induced vibration of flexible cylinders", Journal of Sound and Vibration 433 (2018) 29-54.
14. Peek, R., Witz, M. and Vedeld, K. (2021) “Dynamics of a Pipeline Span on an Elastic Seabed,” Applied Ocean Research 111 (2021) 102407.
15. Bruschi, R. and Vitali, L. (1991) "Large-Amplitude Oscillations of Geometrically Nonlinear Elastic Beams Subjected to Hydrodynamic Excitation," Journal of Offshore Mechanics and Arctic Engineering, ASME, Vol. 113, May 1991, pp. 92-104.
16. Ma, L., Resvanis, T.L. and Vandiver, J.K. (2021) "Enhancing Machine Learning Models with Prior Physical Knowledge to Aid in VIV Response Prediction," Proceedings of the ASME 2021 40th International Conference on Ocean, Offshore and Arctic Engineering," OMAE2021 Virtual Conference: June 21 - June 30, 2021, OMAE2021-62145.
17. Potts, AE, Potts, DA, Marcollo, H, & Jayasinghe, K. "Strouhal Number for VIV Excitation of Long Slender Structures." Proceedings of the ASME 2018 37th International Conference on Ocean, Offshore and Arctic Engineering. Volume 5: Pipelines, Risers, and Subsea Systems. Madrid, Spain. June 17–22, 2018. V005T04A073.
18. Blevins RD, Coughran CS. Experimental Investigation of Vortex-Induced Vibration in One and Two Dimensions With Variable Mass, Damping, and Reynolds Number. ASME. J. Fluids Eng. 2009;131(10):101202-101202-7. doi:10.1115/1.3222904.
19. Tognarelli, M.A., Slocum, S.T., Frank, W.R., Campbell, R.B. (2004) "VIV Response of a Long Flexible Cylinder in Uniform and Linearly Sheared Currents," Paper No. OTC 16338, Offshore Technology Conference, Houston, Texas, 3-6 May 2004.
20. "Vortex Induced Vibration Data Repository," © Copyright 2007 VIV Data Repository Contributors; Site hosted by Center for Ocean Engineering, MIT, Cambridge, MA, USA-02139, http://web.mit.edu/towtank/www/vivdr/index.html
21. Passano, E, Larsen, CM, & Wu, J. "VIV of Free Spanning Pipelines: Comparison of Response From Semi-Empirical Code to Model Tests." Proceedings of the ASME 2010 29th International Conference on Ocean, Offshore and Arctic Engineering. 29th International Conference on Ocean, Offshore and Arctic Engineering: Volume 6. Shanghai, China. June 6–11, 2010. pp. 567-577.
22. Rao, Z., Vandiver, J.K., Jhingran, V., and Sequeiros, O. (2012) " The effect of exposure length on vortex induced vibration of flexible cylinders," Proceedings of the ASME 31th International Conference on Offshore Mechanics and Arctic Engineering, June 10-15, 2012, Rio de Janeiro, Brazil, Paper No. OMAE2012-83273.
23. Lie, H., Braaten, H., Jhingran, V.G., Sequeiros, O. and Vandiver, K. (2012) " Comprehensive Riser VIV Model Tests in Uniform and Sheared Flow," Proceedings of the ASME 31th International Conference on Offshore Mechanics and Arctic Engineering, June 10-15, 2012, Rio de Janeiro, Brazil, Paper No. OMAE2012-84055.

24. Wu, J., et al. (2021) “Forced Vibrations Tests for In-Line Vortex-Induced Vibration to Assess Partially Strake-Covered Pipeline Spans,” Journal of Offshore Mechanics and Arctic Engineering (JOMAE), ASME, published online 10 Nov. 2020, Vol. 143, June 2021.
25. Downing, S.D., Socie, D.F. (1982) “Simple rainflow counting algorithms,” International Journal of Fatigue, Volume 4, Issue 1, January, 31-4.
26. Yin, D., Lie, H., and Baarholm, R. J. "Prototype Reynolds Number Vortex-Induced Vibration Tests on a Full-Scale Rigid Riser." ASME. J. Offshore Mech. Arct. Eng. February 2018; 140(1): 011702.

12 Appendix A – Details of the Rainflow Algorithm Used

The rainflow algorithm used in processing the VIV test data is “Algorithm 1” from [25]. This requires a series of local extreme values of the stresses or strains as input. The data “must be rearranged to begin and end with the maximum peak (or minimum valley)” [25]. Details on how this rearrangement is performed are not fully defined in [25]. If the record is long, different reasonable ways of handling such details should give much the same results. However, for the sake of more accurate reproducibility of the reported results, these details are given here.

For the example considered in Fig. 2 of [25], the first extreme value is a peak and the last a valley. Therefore, upon rearrangement, the valley at the end of the original record is followed by the peak originally at the beginning. This is as it should be: a peak followed by a valley or vice-versa. However, if the first and last extreme in the record were a peak, and the data were rearranged in the same way, it is not clear whether the algorithm would work as intended: After rearrangement, the set of extremes used in the algorithm would contain a peak followed by a peak, rather than having peaks and valleys always alternating. The procedure described below avoids this by working with all data before selecting only the local extreme values:

1) Based on engineering judgment, only the part of the test record representing steady-state VIV response is selected.
2) The rearrangement of the data is done before extracting the extreme values. The rearranged data start with the maximum peak, followed by the steady-state data after the maximum peak, followed by the steady-state data from the beginning to the maximum peak. Thus, the maximum peak is included at the end as well as at the beginning of the rearranged record.
3) From these data, local extreme values are extracted. They include the maximum peak at the beginning and end of the rearranged data, and a local peak and/or valley that may arise in the rearranged data at discontinuity arising from the transition from the last to the first point of the original record, as well as all other local extremes also present in the original steady-state data.

To the extent that local extremes arising at the aforementioned discontinuity may be artificial, this process may slightly overestimate the fatigue damage, but for a sufficiently long segment of steady-state data that should hardly affect the estimated mean fatigue damage rate.

13 Appendix B – Effect of Axial Restraint on Natural Frequencies

The VIV tests considered all involve simply-supported spans with an axial restraint of stiffness k_x. This appendix presents approximate expressions for the effect of the axial stiffness k_x on the natural frequencies of the span, considering also the static displacements due to the combined action of the (vertical) submerged pipe weight $q_g = (c_{pipe} – 1)\, m_{dw}\, g$, and the static component of hydrodynamic force which is assumed to be constant and horizontal, given by $q_d = ½\, \rho\, U^2\, D\, c_d$, where c_d is the drag coefficient. In reality, the drag coefficient varies along the length of the span depending on local VIV amplitude, but it is assumed to be constant, as an approximation. Here “static component” means the average value in time during the VIV test.

This appendix uses the same nomenclature as the main body of the paper. (See Section 2.)

As in Section 2, moderately large displacements are considered. This is a good approximation as long as the rotations remain small compared to 1 radian. The displacements need not be small compared to the pipe diameter, but must be small compared to the span length. For the modal analysis, linearization is applied about the static equilibrium configuration under gravity and drag loads. I.e. nonlinearity in the dynamic response is not considered. This approximation also applies when modes are calculated by finite element analysis.

Since in the VIV tests considered that axial force is always tensile (i.e. $N > 0$), only that case is considered here.

The combination of gravity and drag force causes the pipe to hang in an inclined plane at an angle $\theta = \mathrm{atan}(q_d/q_g)$ from vertical. This will be referred to as the static plane. The modes are then not horizontal and vertical but rather in the static plane and normal to it. Here attention is focused on the in-plane modes. The out-of-plane modes are not affected by the axial stiffness k_x.

When $q_d \ll q_g$, the in-plane modes converge to the cross flow modes, and the out-of-plane modes converge to the in line modes.

13.1 Static Solution in the Static Plane

The governing equation for the transverse displacement v in the static plane is

$$EI\, v_{,xxxx} - N\, v_{,xx} = q_s \quad \forall\ x \in (-a,a) \tag{26}$$

where x denotes the axial coordinate, ranging from $x = -L/2$ at the left shoulder to $x = L/2$ at the right shoulder; the in-plane displacement v is taken to be positive in the direction of the loading; and

$$a = L/2, \qquad q_s = (q_g^2 + q_d^2)^{1/2} \tag{27}$$

(In a convenient normalized form Eq. (27) can be written as $\bar{v}_{,\bar{x}\bar{x}\bar{x}\bar{x}} - \bar{v}_{,\bar{x}\bar{x}} = 1$, where $\bar{x}$ and $\bar{v}$ are normalized values of x and v, obtained by dividing v and x by unit values given by $(EI/N)^{1/2}$ and $q_s EI/N^2$, respectively.)

This, together with boundary conditions $v = v_{,xx} = 0$ at $x = \pm L/2$, yields

$$v = \bar{v}\, q_s\, EI/N^2, \quad \bar{v} = \cosh(\bar{x})/\cosh(\bar{a}) + (\bar{a}^2 - \bar{x}^2)/2 - 1 \tag{28}$$

where variables with an overbar are dimensionless, normalized values given by

$$\bar{x} = (N/EI)^{1/2}\, x, \qquad \bar{a} = (N/EI)^{1/2}\, a \tag{29}$$

If the pipe is axially constrained at the ends, the amount by which it becomes longer due to the transverse displacements v is given by

$$g = ½ \int_{[-a,a]} v_{,x}^2\, dx = \bar{g}\, q_s^2\, EI^{1.5}/N^{3.5} \tag{30}$$

where

$$\bar{g} = ½ \int_{[-\bar{a},\bar{a}]} \bar{v}_{,\bar{x}}^2\, d\bar{x} = [\sinh(2\bar{a}) - 2\bar{a}]/[4\cosh(\bar{a})^2)] + 2\,[\tanh(\bar{a}) - \bar{a}] + \bar{a}^3/3 \tag{31}$$

For numerical calculations for $\bar{a} \le 0.15$, $\bar{g}$ is evaluated from its Taylor series expansion about $\bar{a}=0$, instead of from Eq. (31), to avoid numerical truncation errors. (The leading term in the Taylor series is $17\,\bar{a}^7/315$, and terms up to and including that of order $\bar{a}^{15}$ are included when evaluating the series numerically.)

Now, considering that only one end is axially fixed, and the other is restrained by an axial spring of stiffness k_x, the relationship between the geometric elongation g and the axial force can be written as

$$N = N_0 + g\, EA/L_{ea}\,, \quad L_{ea} = L + EA/k_x \tag{32}$$

where N_0 denotes the axial force before application of the transverse load q_s due to gravity and drag. In this paper these results have been used as follows: (a) Calculate N_0 from Eq. (32) using the measured axial force N under gravity loads alone (i.e. using $q_s=q_g$, $N=N_g$). (b) Use the time-averaged, measured axial force N under flowing conditions to obtain g from Eq. (32). This is the g value under flowing conditions. (c) Obtain q_s from Eq. (30). (d) Obtain $q_d = (q_s^2 - q_g^2)^{1/2}$. (e) Obtain an effective value of the drag coefficient from $c_d = 2q_d/(\rho\, U^2\, D)$. Thus, an effective value of the drag coefficient is calculated for each of the VIV tests, based on the axial force measurements.

It must be recognized that the time-averaging involves an approximation: to the extent that the relationship between the drag force and the axial force is nonlinear, the time-average for the axial force will not be exactly equal to the axial force obtained if the time-average of the drag force is applied as a static load. Hence, the drag coefficients obtained by this calculation should be used with care.

It is expected that the axial tension N increases due to the flow, i.e. that $N > N_g$. However, due to experimental errors, and/or violation of the assumptions of this analysis, that was not the case for all tests considered. For such cases, the effective drag coefficient could not be calculated. For the other cases, the values are shown in Figure 6.5 as a function of the ratio of time-averaged axial force during under flowing conditions during the test N divided by the axial force N_g in still water conditions under gravity loads only. In most cases this yields a reasonable value of the drag coefficient between 1 and 1.5, but when the relative increase in axial force due to the flow is small (i.e. N/N_g close to 1), the results become very sensitive to small errors in measurement of the axial force, or other effects such as temperature changes that could also affect the axial force. These effects are the most likely reason for the increase in scatter of the c_d values where N/N_g is close to 1. For instance, the point with c_d above 18 comes from ExxonMobil Test No. 1103, where the axial force increased from $N_g = 710.7$ N to N = 712.9 N due to the flow. (Note that cases where $N/N_g < 1$ was measured are not included in the plot because c_d values for such cases are undefined. For $N/N_g = 1$, the calculation yields $c_d = 0$.) For larger axial force ratios N/N_g, where the results can be expected to be more reliable. In that range, the results do show a consistently higher drag coefficient for the rough pipe (“Pipe 3 Rough”).

13.2 Analytical Natural Frequencies & Mode Shapes

The out-of-plane mode shapes ϕ and natural frequencies ω_u are given by

$$\phi = \sin(n\pi\,(1/2+x/L)),\quad \omega_u^2 = (n\pi/L)^2\,[(n\pi/L)^2\,EI + N]/m_{eff} \tag{33}$$

where n denotes the mode number, which is the same as the number of lobes. For the in-plane direction, the Rayleigh Ritz approximation of [14] is used to account arch action. Thereby the effect of arch action on the transverse modal displacements and the axial inertia are neglected, to obtain natural frequencies given by

$$\omega = (\omega_u^2 + \omega_{arch}^2)^{1/2},\quad \omega_{arch}^2 = EA\, I_{v'\phi'}^2/(L_{ea}\, m\, I_{\phi\phi}) \tag{34}$$

$$I_{v'\phi'} = \int_{[-a,a]} v_{,x}\, \phi_{,x}\, dx,\quad I_{\phi\phi} = \int_{[-a,a]} \phi^2\, dx \tag{35}$$

Evaluating these integrals yields

$$I_{v'\phi'} = \bar{I}_{v'\phi'}\, q_s\, EI^{1/2}/N^{3/2},\quad I_{\phi\phi} = a \tag{36}$$

where

$$\bar{I}_{v'\phi'} = 2/[\bar{n}(1+\bar{n}^2)],\quad \bar{n} = n\pi/\bar{L},\quad \bar{L} = L(N/EI)^{1/2} \tag{37}$$

The result for $\bar{I}_{v'\phi'}$ is only valid for odd mode numbers n. For even n, the mode is antisymmetric, $\bar{I}_{v'\phi'} = 0$, and there is no arch action.

The strain associated with (unit amplitude) displacements ϕ is

$$\epsilon_t = \pm R_\epsilon\,(n\pi/L)^2 \sin(n\pi\,(1/2+x/L)) + I_{v'\phi'}/L_{ea} \tag{38}$$

where ϵ_t denotes the total dynamic strain including bending and axial components, and ± means plus for the side of the pipe towards which the load q_s acts, and minus for the opposite side. Thus, at the lobe of the mode closest to the shoulders, the axial strain is in phase with the bending stress at the side towards which the load q_s acts.

This completes definition of the effect of arch action on the natural frequencies for the VIV test setups considered, according to the approximation in [14].

14 Appendix C – Accuracy of Scaling Approximations

The scaling assumptions of Section 2 become approximations when they are not satisfied exactly. They include the basic hydrodynamic approximations, (1) to (3), the basic structural approximations,

(4) to (7), and the extended scaling Approximations, (8) and (9). In this appendix, the accuracy of the basic Approximations, (1) to (7), is assessed by defining and calculating dimensionless indicators of the scaling errors.

14.1 Basic Hydrodynamic Approximations

For the compressibility (1) indicator is the Mach number U/c_p. It is small compared to 1 for all cases considered in this paper, as required.

For the viscosity (2), the indicator is the Reynolds number UD/ν. Its effect is sometimes assessed by looking at its effect on the drag coefficient of a rigidly supported cylinder in the flow for which experimental data are available for a large range of Reynolds numbers [26]. It was shown that drag coefficient was sensitive to both Reynolds number and surface roughness ratio. For the cylinder model with surface roughness ratio 5.3×10^{-5}, it was shown a drag crisis in the range $2 \times 10^5 < UD/\nu < 3 \times 10^5$ with roughly constant drag before or after the drag crisis but there is no guarantee that little effect of the Reynolds number on the drag coefficient for the rigidly supported cylinder also means little effect on the VIV response. Achieving at least representative Reynolds numbers is and remains a challenge in VIV testing, since it is difficult and expensive to achieve high Reynolds numbers in VIV tests, especially where the test also aims for high-mode (i.e. high $\tilde{L}$) response.

The Reynolds numbers for the selected tests of Section 6 are shown in Figure 14.1 together with $\tilde{\epsilon}_e$ and in Figure 6.4 together with $\tilde{L}$. They range from 3500 to 112500. According to fits to a large set of data developed in [2], the response is 8%, 4% and 26% higher at the upper end of this range than at the lower end, for “for the mean RMS cross flow, mean RMS in line, and maximum RMS cross flow displacements,” respectively. (In the terminology of [2], “mean RMS” means take the root-mean-square (“RMS”) value in time, then take the average of those RMS values along the span.) For the data in [2] not only the Reynolds number are varied but also other test conditions, which was not accounted for. For instance, it could be that their tests with higher Reynolds number also involved higher mode response, i.e. higher $\tilde{L}$. In that case any effect of $\tilde{L}$ would have been included in the Reynolds number effect according to the fit in [2]. Indeed, recent work [16], using the Shell data for Pipe 2 and 3 suggests that the response tends to increase with increasing Reynolds number, until this causes a change in the mode. It certainly seems reasonable that this could be so, but one must be careful, not to deduce too much from limited data: for the test data considered in [16], increasing Reynolds number means increasing current velocity, or jumping from the 30mm diameter of Pipe 2 to the 80mm diameter of Pipe 3, where in addition most of the Pipe 3 tests are on rough pipe as opposed to smooth pipe used for Pipe 2.

Considering the limitations in available data, a practical approach is to first carry out the assessment with the best available data without enforcing Reynolds number similarity, and then correct for Reynolds number effects, or at least account uncertainty associated with it, using the data available for the larger Reynolds number even if other similarity conditions are not satisfied. This paper only describes the first of these steps.

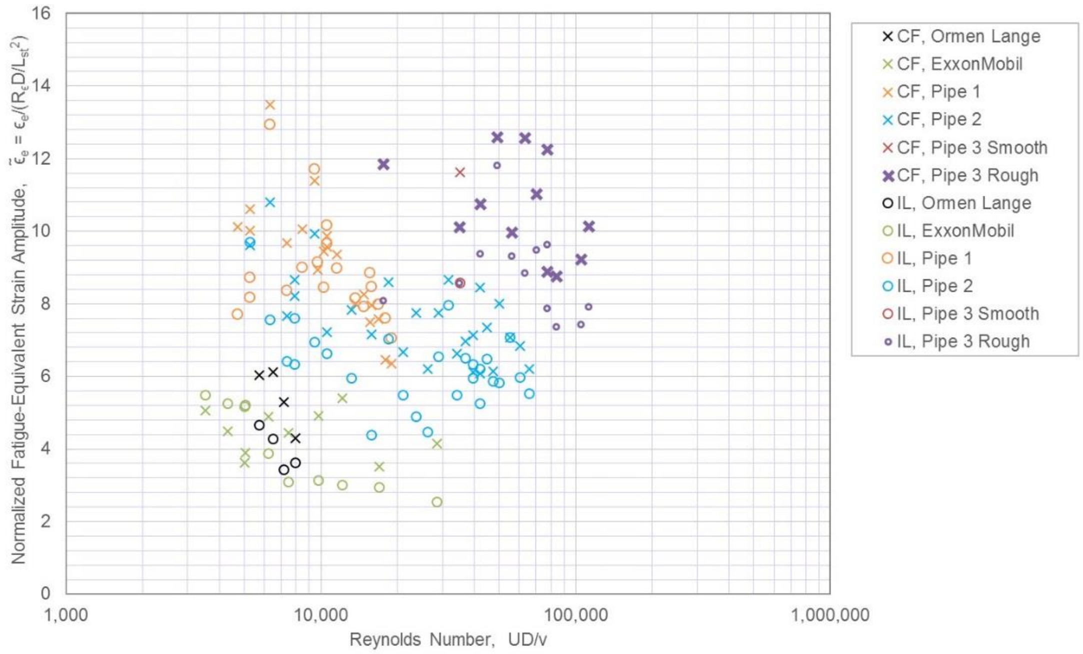

Figure 14.1 Reynolds numbers for the selected tests from Section 6.1

The local action approximation (3) that the hydrodynamic force at any location along the pipe depends on the motion at that location only and not on the motion at adjacent locations is necessary to allow similarity to be satisfied even where L/D ratios are different. It requires the changes in motion along the length of the pipe to be small compared to D. A good measure of a typical distance over which the motion changes along the length of the pipe is the Strouhal half wavelength L_{st}. Thus D/L_{st} should be small compared to 1. This is satisfied for all selected tests. The highest value of D/L_{st} is 0.02. However, a small value of D/L_{st} does not guarantee that local action will be a good approximation. E.g. an aleatory three-dimensional turbulence component that is not deterministically determined by the pipe motion could give rise to forces that vary along the length of the pipe even for an infinitely long rigid cylinder undergoing the same motion everywhere. On the other hand, local action is also implicitly assumed in VIV response functions, such as those used in F105 [3], where it is assumed that the VIV amplitude depends on reduced velocity and damping but not on D/L. Vivana [4] also uses this assumption for the time domain version, as well as the frequency domain one. To the author's knowledge only fully three-dimensional CFD analyses such as [9] do not embody the local action assumption.

14.2 Basic Structural Approximations

The basic structural Approximations (4) to (7) are those that enable to use of the equations for a linearly elastic Euler-Bernoulli beam with moderate deflections at constant axial force, i.e. the use of Eq. (5).

These approximations are assessed for *reference vibrations* defined as vibrations of amplitude[3] D at the Strouhal frequency f_{st} and wavelength $2L_{st}$. For such reference vibrations, the normalized bending strain is $\tilde{\epsilon} = \tilde{\epsilon}_e = \pi^2 \cong 10$. The dynamic rotation amplitude at the nodes is $\pi D/L_{st}$, which has a maximum value of 0.06 radians for the selected VIV tests. A small D/L_{st} required for local action means that the dynamic rotation amplitudes and the effect of shear deformations are also small.

That the pipe remains linearly elastic (4) is best checked for the model based on measured values of the strains and for the prototype based on the stresses calculated by scaling. The polymer pipes used in the VIV tests all have high yield strains and are expected to have remained elastic for all tests.

[3] Where amplitude varies along the length of the pipe and reference is made to a single amplitude it means the amplitude at the location(s) along the span where it is highest.

Not only the dynamic rotations but also the static rotations must be small. For the VIV tests, the static end rotations have been calculated with the formulation of Appendix B, and tests for which this exceeds 0.4 radians are excluded as illustrated in Figure 6.2, to limit the error from using the theory for moderately large deflections.

A typical steel catenary riser ("SCR") is welded as a straight pipe but, as it hangs under gravity loads, it is close to horizontal at the touch-down point and close to vertical at the hang-off point. This means that the static relative end-to-end rotation is close to $\pi/2$, i.e. not small compared 1. Thus, the small rotations scaling Assumption (5) is violated for SCRs. Another difficulty for SCRs is that the axial force and current velocity changes along its length. Although it may be possible to extend the scaling approximations to account for changing axial force along the length of the riser when such changes are slow occurs over large distances compared to L_{st}, such extension is beyond the scope for this paper. On the other hand, there is no scaling approximation to deal with the changing current velocity along the length of the riser. Changing velocity should be reproduced in the VIV test, as is done with the rotating rig of [19] and [23].

Having dealt with the basic structural approximations regarding rotations, shear deformations and linearly elastic behavior only leaves the Assumptions (6) and (7) that justify the constant axial force in Eq. (5).

The most direct indicator of axial force changes are the measurements thereof, and in particular the dynamic amplitude of the axial force, N_{dyn}. The axial force itself does not affect VIV. Only its tendency to straighten the pipe affects the transverse pipe displacements which in turn affects VIV. The stiffness to resist out-of-straightness at the Strouhal wavelength $2L_{st}$, is $(\pi/L_{st})^4$ EI + $(\pi/L_{st})^2$ $(N+N_{dyn})$. The relative change in this stiffness due to the presence of the dynamic component is defined as ψ_N as given in Eq. (22). Only tests with $\psi_N \leq 0.1$ are selected, as illustrated in Figure 6.1. This means that $N_{dyn} \leq 0.1\ N_{seq}$ where N_{seq} is the stiffness-equivalent axial force given in Eq. (23).

Even when N_{dyn} is small, it is conceivable that the stiffness from arch action suppresses a mode that would otherwise be excited. This appears to have been the case for some of the Ormen Lange tests where arch action results in a large increase in the natural frequency of mode 1 (see Figure 6.1). To quantify this, two additional indicators are used: the relative increase in natural frequency due to arch action for mode 1 and for the symmetric mode for which the natural frequency not including arch action is closest to the Strouhal frequency, denoted by $\psi_{arch,1}$ and $\psi_{arch,st}$, respectively. For the latter, the limit $\psi_{arch,st} \leq 0.1$ is applied to select the test data, as illustrated in Figure 6.1.

Arch action arises when one linearizes the structural resistance about the static equilibrium configuration, as opposed to the fully unloaded and stress-free configuration in which the pipe is straight. Thus, it arises from the nonlinear pipe response to the total loading. However, there is also geometric nonlinearity in the dynamic part of the structural response itself. That nonlinearity arises from the second term in the approximate strain-displacement relation for moderately large deflections given by:

$$\epsilon_{c,dyn} = u_{dyn}' + \mathbf{v}'.\mathbf{w}' + \tfrac{1}{2}\, \mathbf{w}'.\mathbf{w}' \tag{39}$$

where $\epsilon_{c,dyn}$ is the dynamic part of the axial strain at the centroid of the pipe, u_{dyn} is the dynamic part of the axial displacement, and **v** and **w** are the static and dynamic parts respectively, of the transverse (lateral and vertical) displacement.

If the dynamic axial force is indeed zero, as assumed, then $\epsilon_{c,dyn}$=0, and integrating Eq. (39) over the span and considering that one end is axially fixed yields a displacement at the other end of

$$g_{dyn} = \int_{span} (\mathbf{v}'.\mathbf{w}' + \tfrac{1}{2}\, \mathbf{w}'.\mathbf{w}')\, dx \tag{40}$$

where g_{dyn} is positive when the displacement is inwards towards the span; g_{dyn} also represents the amount by which the pipe becomes longer over the span due to the dynamic transverse displacements if it is axially restrained at both ends. In reality the pipe is neither axially fully free nor fully fixed at the ends, so that

$$N_{dyn} = (EA/L_{ea})\, g_{dyn} \tag{41}$$

The approximate formulation used for arch action accounts for the first (linear) term in the expression for g_{dyn} but not for the second (nonlinear one). The dynamic axial force due to the nonlinear term thus becomes:

$$N_{nl} = ½ (EA/L_{ea}) \int_{span} \mathbf{w}'.\mathbf{w}' \, dx \tag{42}$$

Evaluating this for the reference vibrations with the assumption that $\tilde{L} = L/L_{st}$ is an integer (so that the Strouhal wavelength satisfies the simply supported boundary conditions), and dividing N_{nl} by the stiffness-equivalent axial force N_{seq} yields the following indicator of the importance of this nonlinear effect

$$\psi_{nl} = N_{nl}/N_{seq} = ¼ (D^2 EA/EI)(L/L_{ea})/(1 + \tilde{N}) \tag{43}$$

For the reference vibrations N_{nl} oscillates between zero and ψ_{nl} N_{seq} at double the Strouhal frequency. Thus, the dynamic amplitude of N_{nl} itself is only ½ ψ_{nl} N_{seq}, and the nonlinearity affects the average axial force by the same amount.

The values of ψ_{nl} for the selected VIV test data range from 0.0004 to 0.15 with the highest values for the Ormen Lange (OL) tests, which are in the range 0.13 to 0.15. This is because in the Ormen Lange tests the axial spring was seen as an important element to satisfy similarity with a prototype, whereas for the other tests the aim was to use a low axial spring stiffness so that the axial force could remain more or less constant. For the other (not OL) tests the maximum value of ψ_{nl} is 0.08. These values of ψ_{nl} indicate that this nonlinear effect at least is not large for the VIV test data.

Up to this point, arch action and the dynamic geometric nonlinearity are addressed under the assumption adopted in [14] that the axial force is constant over the length of the span (though changing in time) and that Eq. (41) applies for the relationship between this axial force and the amount g by which the pipe becomes longer over the span due to the transverse displacements. This follows from momentum balance in the axial direction if the behavior in the axial direction is quasi static. I.e., that with prescribed transverse displacements, using statics to determine the axial force is accurate. For this, the axial inertia must be negligible, as per Assumption (7). Two additional indicators, ψ_{ai1} and ψ_{ai2}, are defined for the axial inertia.

In the first, the frequency of axial modes[4] is compared to the Strouhal frequency. If a straight pipe is axially constrained at one end of the span and free at the other, the natural frequency of the first axial mode is ¼ $(EA/m_{pw})^{1/2}/L$. For static conditions axially this frequency should be large compared to the Strouhal frequency. I.e., the indicator

$$\psi_{ai1} = 4 \, L \, f_{st} \, (m_{pw}/EA)^{1/2} \tag{44}$$

should be small compared to 1. Values of ψ_{ai1} for the VIV test range from 0.025 to 0.035 for OL, and 0.04 to 0.31 for EM. For these values, significant dynamic amplification of the axial response is not expected. For the Shell-sponsored (Pipe 1 to 3) tests, the clump weights strongly change the axial response as discussed in Section 14.3.

The second axial inertia indicator (ψ_{ai2}), arises because ψ_{ai1} is not sufficient: If $EA \rightarrow \infty$, then $\psi_{ai1} \rightarrow 0$, but inertia forces could still produce significant changes in axial force. To understand how significant under such circumstances, it is assumed that $\epsilon_{c,dyn} = 0$ in Eq. (39), since $EA \rightarrow \infty$. For given transverse displacements, the equation can then be integrated to determine the dynamic axial displacement u_{dyn}. This is done for the reference vibrations, assuming $u_{dyn} = 0$ at the axially fixed end, that $\tilde{L}$ is an integer (to simplify the algebra), and considering only the nonlinear ($\mathbf{w}'.\mathbf{w}'$) term, to get u_{dyn} for all (x,t) and its time derivatives $\dot{u}_{dyn}$ and $\ddot{u}_{dyn}$. Then the axial momentum equation $\Delta N' = m_{pw} \ddot{u}_{dyn}$ is solved for the change in axial force ΔN due to these inertial effects, with the boundary condition that $\Delta N=0$ at the axially-free end. Finally, the error indicator is written as $\psi_{ai2} = \Delta N_{max}/N_{seq}$, where ΔN_{max} denotes the maximum absolute value of ΔN over space and time. This leads to

$$\psi_{ai2} = (\pi^4/4) \, \tilde{L}^2 \, (D/L_{st})^2 \tag{45}$$

---

[4] Here "axial mode" means a vibration mode that arises when the pipe is restrained in the transverse direction. For the beam theory for moderately large deflections used, this is the same as the frequency of modes involving purely axial displacements when the pipe is straight.

Evaluating ψ_{ai2} for the test data yields ranges of 0.001 to 0.02 for OL, and 0.004 to 0.34 for EM. Pipes 1 to 3 are addressed in Section 14.3.

The axial inertia indicators ψ_{ai1} and ψ_{ai2} are only important if arch action and/or dynamic nonlinearity are important without axial inertia. More precisely, ψ_{ai1} and ψ_{ai2} need to be small so that the approximation used in deriving indicators $\psi_{arch,1}$, $\psi_{arch,st}$, and ψ_{nl} is valid, but large ψ_{ai1} and/or ψ_{ai2} values do not necessarily mean a large violation of the scaling assumptions.

14.3 Axial Inertia of Clump Weights for Pipes 1 to 3

The Shell-sponsored tests (Pipe 1 to 3) include 500kg clump weights at the end of the pipe. In lieu of a very stiff test rig, this is intended to prevent transverse displacements at the ends to achieve the simply supported boundary condition. However, the clump weights also add much axial inertia, because the clumps also undergo the same axial displacement as the ends of the pipe. (The hinges that allow relative rotations in the two bending directions are between the pipe and the clump weights.) To calculate ψ_{ai1}, an axial vibration mode is considered in which the clump weights at each end move in opposite directions, restrained mainly by the axial stiffness of the pipe. The natural frequency for this mode is approximately $(2EA/(Lm_{clump}))^{1/2}/(2\pi)$, where m_{clump} = 500kg is the mass of the clump weights used. (The hydrodynamic added mass has been neglected for the clump weights, as is the mass of the pipe, and the axial stiffness at the ends, including the end considered to be fully restrained in the static analysis.) This leads frequencies of 2.6, 4.6 and 4.6 Hz for Shell pipes 1 to 3, respectively. The value of ψ_{ai1} then becomes

$$\psi_{ai1,clump} = 2\pi\, f_{st}(Lm_{clump}/(2EA))^{1/2} \qquad (46)$$

If $\psi_{ai1,clump} \ll 1$, the axial response is quasi static. If $\psi_{ai1,clump} \gg 1$, the clump mass is so large that it suppresses axial movements at the ends. The actual values of $\psi_{ai1,clump}$ for the selected tests range from 2.9 to 11 for Pipe 1, from 0.29 to 3.6 for Pipe 2, and 0.13 to 0.88 for Pipe 3. Thus, there may be some tests for Pipes 2 and 3 for which the axial response might be approximated as quasi static, but certainly not all. I.e. the approximation of negligible axial inertia used to quantify the effect of arch action and geometric nonlinearity in the dynamic response is not valid for Pipe 1, nor for a number tests on Pipes 2 and 3. It means that the values of ψ_{nl}, $\psi_{arch,1}$, and $\psi_{arch,st}$ calculated above are not valid for Pipe 1 and a number tests on Pipes 2 and 3. For such cases, the response is more complicated, with axial dynamic playing a role. There could also be significant structural mode interactions due to the geometric nonlinearity in Eq. (39).

At the other extreme, for tests $\psi_{ai1,clump} \gg 1$ means axially fixed conditions at the ends for the dynamic response. For this, ψ_{nl}, $\psi_{arch,1}$, and $\psi_{arch,st}$ can readily be recalculated by setting L_{ea}=L. The results are shown in Table 14.1. They indicate that nonlinearity and arch action could be important for Pipes 1 to 3, even though they hardly are when axial inertia including that of the clump weights is neglected.

In summary, no conclusion can be drawn from the calculated indicators for Pipes 1 to 3 relating to scaling Assumptions (6) and (7) for arch action, geometric nonlinearity, and axial inertia, except that the limit $\psi_N \leq 10\%$ on the dynamic amplitude of the measured axial force should serve to exclude the cases where these effects result in larger dynamic amplitudes of the axial force at the end of the pipe. To satisfy the scaling Approximations (6) and (7), it would have been better to introduce a slider to allow relative axial displacements between the clump weights and the pipe.

	Axially Quasi-Static Behavior						Both Ends Axially Fixed					
	$\psi_{arch,1}$		$\psi_{arch,st}$		ψ_{nl}		$\psi_{arch,1}$		$\psi_{arch,st}$		ψ_{nl}	
	min	max	min	max	min	max	min	max	min	max	min	max
Pipe 1	0.02	0.63	1.e-7	2.e-6	0.002	0.007	1.0	11	1.e-5	2.e-4	0.18	0.65
Pipe 2	0.07	2.6	5.e-6	1.e-3	0.005	0.1	0.61	10	5.e-5	0.01	0.05	1.1
Pipe 3	0.02	0.73	7.e-5	0.02	0.005	0.08	0.19	3.8	8.e-4	0.19	0.06	0.83

Table 14.1 Arch action and nonlinearity indicators for Shell-sponsored VIV tests on Pipe 1 to 3. Values are shown in grey where they are less than 0.1 and thus do not represent a significant scaling

violation or for $\psi_{arch,1}$, since this parameter is not considered directly relevant when higher modes are excited.

15 Appendix D – Adaptation and Interpretation of F105

The DNVGL Recommended Practice for the Assessment of Pipeline Spans [3], provides the algorithm for the calculation of the "F105" results reported in this paper. It is based on modal analysis, response functions to calculate in line and cross flow vibrations amplitudes for each "contributing" mode. It includes rules to determine what modes are contributing, to account for "mode competition", and for cross flow-induced in line vibrations, which have been implemented to produce the reported "F105" results, with the following interpretations and adaptations:

1) Since the intent is to get best estimates of fatigue damage rate, all safety factors are set to 1. This includes safety factors on natural frequencies, damping, stress range, current velocity at onset of VIV, and number of cycles for fatigue damage.
2) Zero structural and soil damping is assumed, since for the model tests the damping is low, but there is uncertainty about exactly how low, and how the damping varies with amplitude and mode number.
3) The turbulence intensity of the incoming flow is taken to be zero, since the models are towed in still water.
4) For the prototype example, the stiffness of the coatings is neglected in the F105 calculation, as well as in the application of the scaling results.
5) The modal analysis is performed using the axial force under flowing conditions based on the static solution of Appendix B. It is not clear whether this is the intended interpretation of "The parameters [including axial force] should be determined for every relevant pipeline condition, i.e. as-laid, flooded, pressure test, operating and shut-down conditions." (F105, Section 6.1.2), but, using the actual static component of the axial force is expected to give more accurate estimates of the fatigue damage rate, than performing the linearization required for modal analysis about the still-water static equilibrium configuration.
6) When arch action is included, the modes are in and normal to the static plane, rather than in line and cross flow. Yet applying F105 requires in line and cross flow modes. To get these, the pipeline is restrained on one direction in order to calculate the modes and frequencies in the other. I.e. in line motion is restrained to calculate the cross flow frequencies and cross flow motion is restrained to calculate the in line frequencies. In practice this amounts to using the vertical static deflection to calculate the cross flow frequencies, and the horizontal static deflection to calculate the in line frequencies. These frequencies are then somewhere in between those of modes in and normal to the static plane. Strictly, according to F105, one might use Appendix A of F105 to handle modes that involve both in line and cross flow motions. However, that is intended mainly for subsea structures, rather than for pipelines.
7) With arch action, the dynamic stresses include an axial component (that is constant over the cross section) included in Eq. (38) in addition to the bending one given in Section 6.6.2 of F105. Combining axial and bending stresses, one cross flow mode may have the highest stresses at the top of the pipe and the other at the bottom. However, for conservative simplicity, it is assumed for any cross section that all cross flow modes produce the highest stresses at the same side of the cross section. This is done by taking the absolute values of the axial and bending terms in Eq. (38), and applied to the in line as well as cross flow modes.